

---

# Stabilizing diode lasers to an ultrastable reference cavity

Stephan Herman Wissenberg

---



München 2017



---

# **Stabilisierung von Diodenlasern auf einen ultrastabilen Referenz-Resonator**

---

Masterarbeit  
an der Fakultät für Physik  
der Ludwig-Maximilians-Universität München  
Max-Planck-Institut für Quantenoptik

vorgelegt von  
Stephan Herman Wissenberg  
aus Traunstein

München, den 21.07.2017



# Contents

<b>Abstract</b>	<b>xi</b>
<b>1 Introduction</b>	<b>1</b>
1.1 Outlook . . . . .	2
<b>2 Resonators</b>	<b>5</b>
2.1 Light propagation . . . . .	5
2.2 ABCD transfer matrix . . . . .	6
2.3 Stability of a resonator . . . . .	7
2.4 Gaussian beams . . . . .	8
2.5 Resonant beams and frequencies of a plano-concave resonator . . . . .	13
2.6 Light fields in optical resonators . . . . .	15
2.7 Measuring the finesse . . . . .	17
<b>3 Laser stabilization</b>	<b>21</b>
3.1 Feedback and control theory . . . . .	22
3.1.1 Feedback . . . . .	23
3.1.2 Examples for control laws . . . . .	24
3.2 PDH locking . . . . .	25
<b>4 Ultrastable reference cavity</b>	<b>31</b>
4.1 Frequency stability of a resonator . . . . .	31
4.1.1 Thermal expansion . . . . .	32
4.1.2 Vibrations . . . . .	33
4.1.3 Pressure fluctuations . . . . .	33
4.2 Design . . . . .	34
4.2.1 The chamber . . . . .	34
4.2.2 Active temperature stabilization . . . . .	36
4.2.3 Passive temperature stabilization . . . . .	38
4.2.4 ULE-cavity . . . . .	38
4.3 Assembling the cavity . . . . .	38
4.3.1 Cleaning vacuum parts . . . . .	39
4.3.2 Assembling the parts . . . . .	40

---

4.3.3	Mirror contamination and second attempt . . . . .	42
4.4	Temperature stability . . . . .	45
4.4.1	Characteristic cooling time . . . . .	45
4.4.2	Temperature stability . . . . .	45
<b>5</b>	<b>Locking procedure and results</b>	<b>49</b>
5.1	Optical setup and components . . . . .	49
5.2	Mode-matching . . . . .	52
5.3	Electronics and setting them up . . . . .	55
5.3.1	Photo detector . . . . .	55
5.3.2	PDD 110/F . . . . .	56
5.3.3	FALC . . . . .	56
<b>6</b>	<b>Unibody Littrow Laser</b>	<b>63</b>
6.1	ECDL . . . . .	63
6.2	Components . . . . .	64
6.2.1	Choosing a laser diode . . . . .	65
6.2.2	Grating . . . . .	66
6.3	Construction . . . . .	67
6.3.1	Assembling tips . . . . .	67
<b>7</b>	<b>Conclusion</b>	<b>69</b>
7.1	Summary . . . . .	69
7.2	Outlook . . . . .	70
	<b>Acknowledgments</b>	<b>77</b>

# List of Figures

1.1	Strontium energy level diagram . . . . .	2
2.1	Schematic drawing of a Fabry-Pérot Resonator . . . . .	6
2.2	ABCD Matrices Illustrated . . . . .	7
2.3	Stability diagram of optical Resonators . . . . .	9
2.4	TEM modes . . . . .	13
2.5	Field transmission of a Fabry-Pérot . . . . .	16
2.6	Ring down time measurement . . . . .	19
2.7	Swept ring down measurement . . . . .	20
3.1	Simple Block Diagram . . . . .	23
3.2	Feedback block diagram . . . . .	25
3.3	Intensity and phase of reflection coefficient . . . . .	26
3.4	PDH setup . . . . .	27
3.5	PDH setup . . . . .	29
4.1	Vacuum housing of reference cavity . . . . .	35
4.2	Inside view of the stable reference cavity . . . . .	37
4.3	Radiation shield before and after plasma cleaning . . . . .	40
4.4	Glued Heater and Thermistor . . . . .	41
4.5	Fabry-Perot cavity on ZERODUR spacer . . . . .	42
4.6	Radiation shield inside the vacuum chamber . . . . .	43
4.7	Assembled copper box with wiring . . . . .	43
4.8	Image of the contaminated mirrors before and after they were cleaned. . . . .	44
4.9	Temperature ring down measurement . . . . .	46
4.10	Temperature disturbance . . . . .	48
5.1	Optical setup on the cavity . . . . .	50
5.2	Custom mirror mount . . . . .	52
5.3	Scan of a free spectral range . . . . .	53
5.4	Control panels PDD 110/F and schematics . . . . .	57
5.5	Measured error signal . . . . .	57
5.6	FALC control panel . . . . .	58
5.7	FALC block diagram . . . . .	58

5.8	Power spectral density of the error signal . . . . .	60
6.1	Schematics of a Littrow Laser . . . . .	64
6.2	Picture of the Littrow laser . . . . .	65

# List of Tables

2.1	Some ABCD transfer matrices . . . . .	7
4.1	CTE of common spacer materials . . . . .	32
4.2	Thermal properties of common vacuum materials . . . . .	36
6.1	List of Laser diodes and gratings for a Littrow laser . . . . .	66



# Abstract

In this thesis, I report on a project to frequency-stabilize diode lasers to an ultrastable frequency reference. This reference system is a high finesse Fabry-Pérot resonator embedded in a vacuum housing that provides  $< 1$  mK temperature stability and isolates the resonator from vibrations. With multiple techniques, we measured the resonators finesse be  $\sim 270\,000$  at 689 nm. We present a compact optical setup that allows locking two diode lasers with wavelengths 689 nm and 698 nm to the same ultrastable frequency reference. In addition, we present a custom diode laser system operating at 633 nm and provide a complete set of instructions that allows building a similar laser for a variety of wavelengths of interest. This work was done in the strontium laboratory in Immanuel Blochs group at MPQ under the supervision of Dr. Sebastian Blatt.



# Chapter 1

## Introduction

Cooling atoms to quantum degeneracy has opened a new field of physics. Ultracold atoms offer a unique platform for studying quantum many-body effects with a high degree of controllability. Nowadays it is possible to load cold atoms into artificial lattices to imitate solid state crystals [1]. The hope is to exploit the universality of quantum mechanics by mapping the properties of a hardly controllable system onto a controllable system. By letting our controllable system evolve we simulate the system which we are interested in, as originally proposed by Feynman [2]. The lattices are created by counter propagating laser beams that form a standing wave. The standing waves create a periodic pattern of potential wells that can capture atoms. In contrast to crystal lattices, lattices composed of light are highly controllable. The light frequency determines the lattice constant and the intensity sets the potential depth.

Alkaline-earth-metals stored in optical lattices offer a wide range of new applications. The two valence electrons result in a rich electronic level structure. Depending on the individual spins of the valence electrons, they form either a singlet (anti parallel spins) or a triplet (parallel spins) state. In fermionic isotopes, the nuclear spin has a non-zero value ( $I \neq 0$ ). Mixing the nuclear spin with the  $^3P_0$  results in a very narrow transition. This “clock transition” connects the ground  $^1S_0$  state to the long-lived triplet  $^3P_0$  state, with both having an electronic angular momentum  $J = 0$ . This combination is the reason for several proposals, including for instance quantum computation schemes [3, 4] and simulating models with  $SU(N)$  symmetry [5], where  $N$  can be as large as 10.

In our experiment, we aim to perform many-body physics with the alkaline-earth metal Strontium. Strontium (Sr) is a great choice for such experiments. In the past years, Sr has been extensively studied in optical lattice clocks [6] and Sr bosonic and fermionic isotopes have been cooled to quantum degeneracy [7]. The knowledge to cool Sr is readily available. A part of the Sr energy level diagram is depicted in Figure 1. Currently we can catch the Sr atoms in a magneto optical trap (MOT) using the broad 461 nm transition from singlet state  $5s^2\ ^1S_0$  to singlet state  $5s5p\ ^1P_1$ . Reference [8] explains the details of how a MOT works. The next step is to load the atoms into the red MOT, cooling the atoms down to a temperature of  $\approx 1\ \mu\text{K}$  [9]. The red MOT exploits the narrow singlet  $5s^2\ ^1S_0$  to triplet  $5s5p\ ^3P_1$  transition.

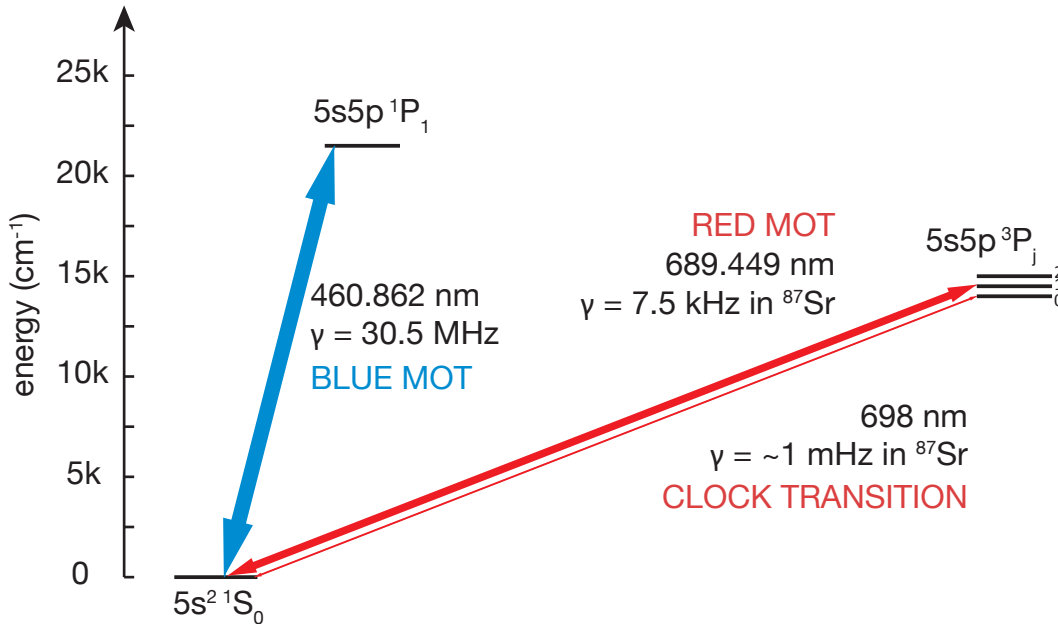


Figure 1.1: Energy level structure of Strontium. Marked are the electronic transitions which are used for cooling Sr and the narrow clock transition.

For the red MOT we need a laser with a linewidth narrower than the 7.5 kHz, which is the linewidth of the transition. To achieve this narrow linewidth with a diode laser, one has to lock the laser to a frequency reference. The same is true for the clock transition, although it is far narrower. This thesis reports on the construction of an ultrastable frequency reference. The frequency reference is used to narrow down the linewidths of the clock laser at 698 nm. Later, it should address the clock transition of  $^{87}\text{Sr}$ . Simultaneously, we lock the red laser at 689 nm to the same reference cavity, which is used to create the red MOT.

## 1.1 Outlook

In this thesis, I report on my work done in the Ultracold Strontium Experiment at the Max-Planck-Institute for Quantum Optics. My main topic was stabilizing two diode lasers to an ultrastable frequency reference. While working on the laser stabilization project, I also built an external cavity diode laser.

Chapter 2 examines the theory of optical resonators and laser beams. A good understanding of the concepts is essential for this thesis. After this section, we have a first look at measurements that were performed to characterize an optical resonator.

In Chapter 3, we first concentrate on control theory and discuss how we can stabilize a physical quantity to a certain value. Using the Pound-Drever-Hall locking scheme, we can reference the laser frequency to an optical resonator and use a feedback loop to stabilize

the laser frequency.

In Chapter 4, we analyze our stable reference system. After talking about the reasons for perturbations and the design of the cavity, we carefully discuss each step of assembling the cavity. At last, we discuss about the isolation of the ultrastable cavity housing against temperature fluctuations.

In Chapter 5 we finally lock the laser to the stable reference cavity. This chapter discusses every optical element in the setup as well as the precise locking procedure. After the laser is locked we will make a rough estimate of the linewidth and see how good our system performs.

Chapter 6 reports on an external cavity diode laser (ECDL) that I built. We will have a look at the design, how it was built and the optical setup of the laser system. This chapter also intends to provide a guideline on how to choose the parts to construct the laser for a certain wavelength.



# Chapter 2

## Resonators

In this chapter we introduce the basic concepts of laser beams and optical resonators as they are of fundamental importance in laser physics. Many good books and reviews can be found on this topic, see for example Ref. [10] or Ref. [11]. In its simplest form an optical resonator consists of two mirrors facing each other (see Figure 2.1). This resonator configuration is known as a Fabry-Pérot cavity and has many different applications in, for instance, interferometry and spectroscopy. In this thesis a Fabry-Pérot cavity is used as a frequency reference for laser stabilization, but to be able to understand how the stabilization scheme works we have to look up the relevant optical concepts. A good starting point is to discuss how light can be treated mathematically and be described in a physical way. This formalism will serve as basis to study important resonator properties and how these properties can be measured experimentally.

### 2.1 Light propagation

How does light propagate from one point  $P_1$  to another point  $P_2$ ? Today we know that visible light is characterized by oscillations of the electromagnetic field with a frequency  $\nu$  in the range of 430-750 THz. These frequencies corresponds to wavelengths  $\lambda$  in the range of 400-700 nm. These wavelengths are so small that for most of the day-to-day observations of how light behaves a very good approximation is letting  $\lambda \rightarrow 0$ . Remembering Fermat's principle that *light travels from  $P_1$  to  $P_2$  along the path that connects those points with the shortest optical length within a certain vicinity* (see Ref. [12, pp. 136-139]). This shortest path is called a light ray. From Fermat's principle follows the reflection law, which states that the angle of incidence is equal to the angle of reflection with respect to the surface normal. Moreover, we can derive Snell's law of refraction, which governs how a light ray is refracted at an interface between two media with index of refraction  $n_1$  and  $n_2$ , respectively. We find (for a derivation see Ref. [13, p. 182-183]) that the angles  $\theta_1$  and  $\theta_2$  are related by

$$n_1 \sin \theta_1 = n_2 \sin \theta_2, \quad (2.1)$$

which becomes

$$n_1 \theta_1 = n_2 \theta_2 \quad (2.2)$$

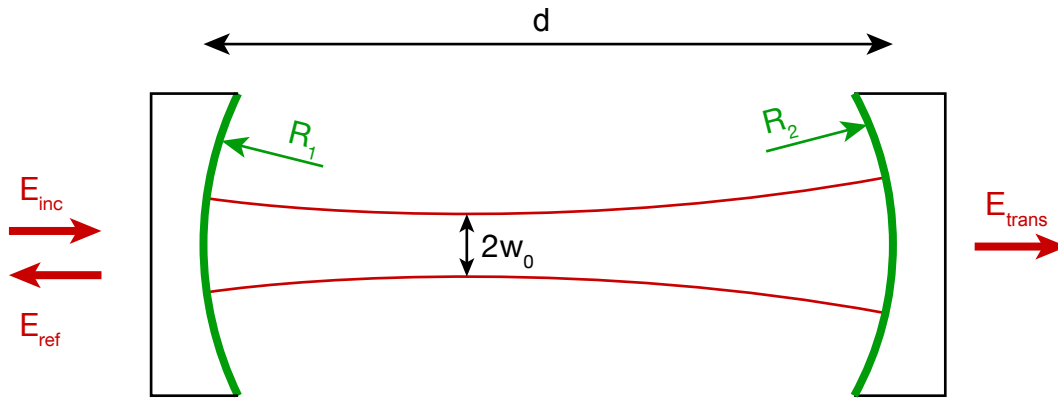


Figure 2.1: This figure illustrates a Fabry-Pérot Resonator, consisting of two mirrors with radius of curvature  $R_1$  and  $R_2$ , respectively. We also indicate the position of the beam waist  $w_0$ .

for  $\theta_{1,2} \ll 1$ , which is known as the paraxial approximation. This formalism for optics is called geometrical optics because the propagation path of light is calculated with the laws of geometry.

## 2.2 ABCD transfer matrix

In geometrical optics the propagation of a ray of light within the plane of incidence is fully described by a set of two parameters at a position  $z_1$  on the optical axis. These parameters are the radial distance to the optical axis  $x_1$  and its slope with respect to the optical axis  $x'_1$ . To determine the beam's properties after it has passed through an optical system, at position  $z_2$  one applies a linear transformation of the following form:

$$\begin{pmatrix} x_2 \\ x'_2 \end{pmatrix} = \begin{pmatrix} A & B \\ C & D \end{pmatrix} \begin{pmatrix} x_1 \\ x'_1 \end{pmatrix}. \quad (2.3)$$

This transformation is also depicted in Figure 2.2. The ABCD-matrix that corresponds to an optical element can be calculated using only Snell's law of refraction together with the paraxial approximation. Table 2.1 lists some of the most commonly used transfer matrices. The first column describes a ray traveling an axial distance  $d$  in an optical medium with homogenous index of refraction  $n$ . The second column is used for a thin lens. If this matrix is applied to a given state, we obtain the state of the beam immediately after the lens. The last ABCD matrix is used for a curved surface; the radius of curvature  $R$  is positive if the center of curvature is on the same side from which the beam is approaching and  $n_1$  ( $n_2$ ) is the index of refraction of the material before (after) the curved surface. The ABCD matrix of a flat interface can be obtained by taking the limit  $R \rightarrow \infty$ . Transfer matrices of more complex optical systems can be calculated by matrix multiplication of the transfer

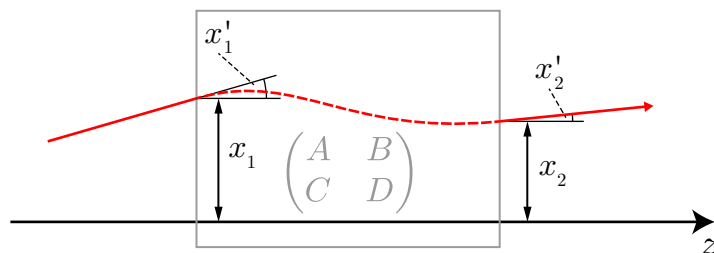


Figure 2.2: Propagation of a ray of light (red) and how it is transformed while passing through an optical system (gray box).

matrices of the individual optical elements.

## 2.3 Stability of a resonator

In an ideal stable resonator with perfect mirrors a light ray would bounce back and forth forever. In other words, stability means that for a resonator there exist  $x_1$  and  $x'_1$ , such that applying the ABCD matrix of the resonator an arbitrary amount of times  $n$  does not lead to diverging values of  $x_n$  and  $x'_n$ .

Having in mind a Fabry-Pérot resonator as in Figure 2.1, we can find the properties of a stable resonator by replacing the mirrors by a periodic sequence of two lenses which have the same focusing power as the mirrors ( $f_{\text{Mirror}} = R/2$ ). Then the ABCD matrix for one full round trip can be written as

$$\begin{pmatrix} A & B \\ C & D \end{pmatrix} = \begin{pmatrix} 1 & 0 \\ -\frac{2}{R_1} & 1 \end{pmatrix} \begin{pmatrix} 1 & d \\ 0 & 1 \end{pmatrix} \begin{pmatrix} 1 & 0 \\ -\frac{2}{R_2} & 1 \end{pmatrix} \begin{pmatrix} 1 & d \\ 0 & 1 \end{pmatrix}, \quad (2.4)$$

assuming that the material between the mirrors has a refractive index of 1. To write the following equations in a nicer form, one usually defines the two parameters

	Distance $d$	Thin lens	Curved surface
$\begin{pmatrix} A & B \\ C & D \end{pmatrix}$	$\begin{pmatrix} 1 & d/n \\ 0 & 1 \end{pmatrix}$	$\begin{pmatrix} 1 & 0 \\ -1/f & 1 \end{pmatrix}$	$\begin{pmatrix} 1 & 0 \\ -\frac{(n_1-n_2)}{n_2 R} & n_1/n_2 \end{pmatrix}$

Table 2.1: A list of some of the most commonly used transfer matrices, describing propagation in free space over distance  $d$ , the focusing of a thin lens with focal length  $f$ , and the refraction at a curved interface (radius  $R$ ) of two media with refractive indices  $n_1$  and  $n_2$ , respectively.

$$g_1 = 1 - \frac{d}{R_1} \quad (2.5)$$

$$g_2 = 1 - \frac{d}{R_2}, \quad (2.6)$$

such that Eqn. (2.4) can be rewritten as

$$\begin{pmatrix} A & B \\ C & D \end{pmatrix} = \begin{pmatrix} 2g_2 - 1 & 2g_2 d \\ \frac{2}{d}(2g_1 g_2 - g_1 - g_2) & 4g_1 g_2 - 2g_2 - 1 \end{pmatrix}. \quad (2.7)$$

To see how a ray of light behaves when the transformation of Eqn. (2.7) is applied  $n$  times, we can use Sylvester's matrix theorem [14]:

$$\begin{pmatrix} A & B \\ C & D \end{pmatrix}^n = \frac{1}{\sin \theta} \begin{pmatrix} A \sin n\theta - \sin(n-1)\theta & B \sin n\theta \\ C \sin n\theta & D \sin n\theta - \sin(n-1)\theta \end{pmatrix}, \quad (2.8)$$

with

$$\cos \theta = \frac{1}{2}(A + D). \quad (2.9)$$

Equation (2.9) leads to the stability criterion  $|A + D| \leq 2$ . We see that if the stability criterion holds,  $\theta$  is real and the individual elements of the transfer matrix are oscillating functions of  $n$  and therefore take the same values over and over again. One can imagine that a ray inside a stable cavity is periodically refocused. In case this inequality does not hold,  $\theta$  becomes imaginary and the transfer matrix consists of hyperbolic functions. Hyperbolic functions diverge for large arguments and so does the distance to the optical axis of a light ray entering this unstable cavity. At one point the diameter of the mirrors will not be large enough and the ray escapes from the cavity.

Using the definitions in Eqns. (2.5) and (2.6), the stability criterion for a resonator can be expressed as

$$0 \leq g_1 g_2 \leq 1. \quad (2.10)$$

In Figure 2.3 this stability criterion is plotted and the result is called a stability diagram, illustrating the regions of stability and instability. For instance it becomes clear that not any cavity near the confocal ( $R_1 = R_2 = d$ ) configuration is stable.

## 2.4 Gaussian beams

The simple analysis in the previous section already gave some useful insights, and for many optical problems a treatment with geometrical optics is fully sufficient. Geometrical optics only break down when the finiteness of the wavelength becomes important. An everyday example are the colorful rings in puddles that form on a rainy day out in the streets when



Here  $k = 2\pi/\lambda$  is called the wave vector. If we define the  $z$ -axis along the axis of beam propagation, a simple solution to (2.12) are plane waves, i.e.  $u = u_0 \exp(-ikz)$ . This solution suggests a beam with a plane phase front that expands infinitely in the  $x$  and  $y$  directions. To obtain a spatially limited beam we make an Ansatz that is still similar to a plane wave, but also includes a slowly varying complex function  $\psi(x, y, z)$  that depends on the Cartesian coordinates:

$$u = \psi(x, y, z) \exp(-ikz). \quad (2.13)$$

Now we will try to find solutions for  $\psi(x, y, z)$  such that  $u$  represents the electric field of a laser beam. We again use the paraxial approximation, and require that the angle between the direction of propagation and the optical axis is small. As a consequence, when inserting Eqn. (2.13) into Eqn. (2.12), we neglect the second derivative with respect to  $z$ . We obtain the paraxial wave equation:

$$\frac{\partial^2 \psi}{\partial x^2} + \frac{\partial^2 \psi}{\partial y^2} - 2ik \frac{\partial \psi}{\partial z} = 0, \quad (2.14)$$

which can be solved by

$$\psi = \exp \left\{ -i \left( P + \frac{k}{2q} r^2 \right) \right\}. \quad (2.15)$$

Here  $r^2 = x^2 + y^2$  is the radial distance to the  $z$ -axis. In Eqn. (2.15), two new parameters emerge: the complex beam parameter  $q$  is responsible for the radial limitation of the field distribution and a curvature in the phase front. The other parameter  $P$  is responsible for the so-called Gouy phase, which we will discuss later. At the moment these two new parameters might appear hard to interpret, but their physical meaning will soon become clear. To find an expression for these two new parameters one simply plugs Eqn. (2.15) into Eqn. (2.14) and by comparing terms of equal power in  $r$  we find:

$$\frac{\partial q}{\partial z} = 1 \quad (2.16)$$

and

$$\frac{\partial P}{\partial z} = -\frac{i}{q}. \quad (2.17)$$

Complex numbers are not very intuitive which is why it is better to write  $q$  as a function of two real beam parameters  $w(z)$  and  $R(z)$ :

$$\frac{1}{q} = \frac{1}{R} - i \frac{\lambda}{\pi w^2}. \quad (2.18)$$

In the beginning this choice seems arbitrary, but it helps to evaluate the complex beam parameter  $q$ . The expression for the electric field we have derived now becomes

$$u = \exp \left\{ -i \left( P(z) + kz + \frac{kr^2}{2R} \right) - \frac{r^2}{w^2} \right\}, \quad (2.19)$$

which can be interpreted clearly: The real part in the exponential of Eqn. (2.19) creates an envelope along the radial distance to the optical axis which has a Gaussian form. The parameter  $w$  is the radial distance at which the field amplitude of the beam decreases to  $1/e$  of its peak at  $r = 0$ . Therefore  $w$  is often referred to as the beam radius. Also the meaning of the parameter  $R$  becomes clear: it is the radius of curvature of the phase front.

To summarize these results: with equation (2.19) we have found a solution to the wave equation that governs the electromagnetic field. To obtain a realistic description of laser beams, we began with plane waves and confined them to a finite extent. The result was a beam that has a Gaussian field profile and a curved phase front. It should be stressed that this solution is only valid for paraxial beams that do not diverge too fast, otherwise our approximation that the field varies only slowly in the  $z$ -direction in Eqn. (2.14) breaks down. The complex beam parameter  $q$  contains all the geometrical information of the beam and can be used to calculate the beam radius  $w$  and the radius of curvature of the phase front  $R$ .

The beam radius has a minimum called the beam waist  $w_0$  and one usually defines the position where the beam waist occurs to be as  $z = 0$ . When the beam radius contracts to a minimum, the radius of curvature of the laser beam diverges and  $q$  becomes completely imaginary:

$$q_0 = i \frac{\pi w_0^2}{\lambda}. \quad (2.20)$$

Another useful quantity to describe a Gaussian beam is the Rayleigh range, which is the distance on the optical axis between the position of the beam waist and the position where the beam radius expands to  $\sqrt{2}w_0$ :

$$z_R = \frac{\pi w_0^2}{\lambda}. \quad (2.21)$$

With Equations (2.18), (2.20) and the definition of the Rayleigh range, the beam radius and the phase front curvature at any arbitrary position  $z$  can be related to the beam waist. We obtain the two relations

$$w(z)^2 = w_0^2 \left[ 1 + \left( \frac{z}{z_R} \right)^2 \right], \quad (2.22)$$

$$R(z) = z \left[ 1 + \left( \frac{z_R}{z} \right)^2 \right]. \quad (2.23)$$

Integrating (2.16) yields

$$q_2 = q_1 + z, \quad (2.24)$$

which connects two different  $q$ -parameters of a beam at two different positions, separated by a distance  $z$ . Equation (2.24) can now be used to write down an expression for  $q$ , which depends only on the distance to the beam waist and the beam waist itself:

$$q = q_0 + z = i \frac{\pi w_0^2}{\lambda} + z. \quad (2.25)$$

Having found this equation for  $q$  we can finally solve equation (2.17) to find the complex phase shift  $P$ :

$$\frac{\partial P}{\partial z} = -\frac{i}{q} = -\frac{i}{z + i \frac{\pi w_0^2}{\lambda}}. \quad (2.26)$$

Integration from the position of the beam waist ( $z = 0$ ) gives

$$iP = \ln \sqrt{1 + \left(\frac{\lambda z}{\pi w_0^2}\right)^2} - i \tan^{-1} \left(\frac{\lambda z}{\pi w_0^2}\right), \quad (2.27)$$

which is straightforward to interpret: the real part of  $iP$  in Eqn. (2.27) introduces the expected decrease in field amplitude, as the Gaussian beam is expanding from the beam waist. The imaginary part adds an additional phase, which is called the Gouy phase. The fundamental Gaussian beam can therefore be written as

$$u(r, z) = \frac{w_0}{w} \exp \left[ -i(kz - \Phi) - r^2 \left( \frac{1}{w^2} + \frac{ik}{2R} \right) \right], \quad (2.28)$$

with the Gouy phase

$$\Phi = \tan^{-1} \left( \frac{\lambda z}{\pi w_0^2} \right). \quad (2.29)$$

Until now only one possible solution to Eqn. (2.14) was discussed, which resulted in a Gaussian intensity shape along the  $x$  and  $y$  axis. Although this solution is a very important, the Gaussian beam is by far not the only one. Indeed, there exists a whole set of solutions which form a complete and orthogonal set of functions. In Cartesian coordinates these solutions can be written as [11]

$$u(x, y, z) = \frac{w_0}{w} H_m \left( \sqrt{2} \frac{x}{w} \right) H_n \left( \sqrt{2} \frac{y}{w} \right) \exp \left[ -i(kz - \Phi(n, m; z)) - i \frac{k}{2q} (x + y)^2 \right], \quad (2.30)$$

where  $H_{m,n}$  are the Hermite polynomials and  $\Phi(n, m; z)$  is again the Gouy phase, but this time in its general form which depends on the transverse mode numbers  $n$  and  $m$ :

$$\Phi = (m + n + 1) \tan^{-1} \left( \frac{\lambda z}{\pi w_0^2} \right). \quad (2.31)$$

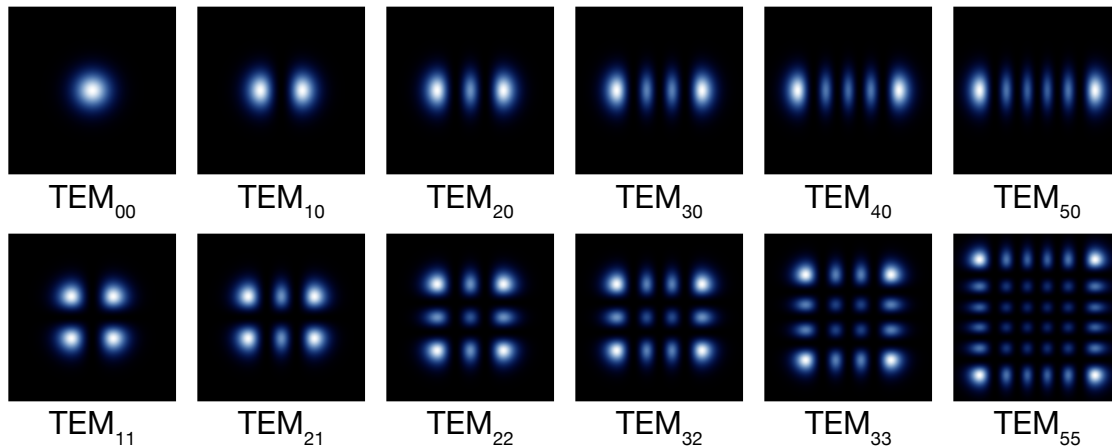


Figure 2.4: This figure shows a few of the lowest TEM modes.

The solutions in Eqn. (2.30) are called transverse electromagnetic ( $\text{TEM}_{nm}$ ) modes and the two numbers  $n$  and  $m$  indicate which mode is meant. For instance, the lowest order  $\text{TEM}_{00}$  mode corresponds to the Gaussian shaped beam which was discussed previously. Figure 2.4 shows several examples of TEM modes.

## 2.5 Resonant beams and frequencies of a plano-concave resonator

Relation (2.24) connects two  $q$ -parameters which are separated by a certain axial distance. This relation already indicates that there is a possibility to obtain the  $q$ -parameter of a laser beam after it has passed through an optical system. And indeed, if one knows the ABCD-transfer matrix of the system, the  $q$ -Parameter  $q_1$  immediately before the system and the  $q$ -parameter  $q_2$  immediately after the system are connected by

$$q_2 = \frac{Aq_1 + B}{Cq_1 + D}, \quad (2.32)$$

which is known as the ABCD law. Here, we only motivate Eqn. (2.32) by noting that the ABCD law leads to Eqn. (2.24) when applying the ABCD matrix of free space. See Ref. [15, pp. 93-94] for a full proof via induction.

We can apply this rule to calculate some properties of a laser beam resonant with an arbitrary stable cavity. We enforce the condition that the  $q$ -parameter replicates after a full round trip

$$q = \frac{Aq + B}{Cq + D} \quad (2.33)$$

together with the ABCD-matrix of a resonator in Eqn. (2.4). Solving this equation yields the  $q$ -parameter of the laser beam after being reflected from the first mirror:

$$\frac{1}{q} = \frac{g_1 - 1}{d} \pm \frac{1}{g_2 d} \sqrt{g_1 g_2 (g_1 g_2 - 1)}. \quad (2.34)$$

Using Eqn. (2.18), we find that the wavefront radius at this point is equal to  $-R_1$  and thus matches the mirror shape. Particularly interesting here is the case of a plano-concave resonator: choosing  $R_1 = \infty$  ( $g_1 = 1$ ) lets the real part of Eqn. (2.34) vanish, which means that the beam waist of this resonator type is located at the plane mirror. The beam waist becomes

$$w_0^2 = \frac{\lambda}{\pi} \sqrt{d(R_2 - d)}. \quad (2.35)$$

The resonator used in this work has exactly this shape and this equation will be very useful later on when we want to couple as much light as possible from the laser into the resonant mode, because we have to “shape” the incident laser beam into the correct form.

To find these relations the only condition we enforced was that the  $q$ -parameter of the beam has to replicate after a full round trip. To determine the resonant frequencies, we have to require that the phase which the beam accumulates in a full round trip is a multiple of  $2\pi$ . Recasting equations (2.30) and (2.31) we can write this condition for the plano-concave resonator as:

$$2\pi l = 2kd - 2(n + m + 1) \tan^{-1} \left( \frac{d}{z_R} \right), \quad (2.36)$$

where  $l$  this time is an integer number. The two contributions to the phase are the phase a plane wave accumulates when traversing a distance  $2d$  plus the Gouy phase for the same distance. Using equations (2.6), (2.21), (2.35) and the trigonometric identity

$$\tan^{-1}(x) = \cos^{-1} \left( \frac{1}{\sqrt{1 + x^2}} \right), \quad (2.37)$$

we can rewrite the resonance condition in Eqn. (2.36) to obtain an expression for the actual frequencies which are resonant with the plano-concave resonator:

$$\nu_{nml} = \frac{k_{nml} c}{2\pi} = \frac{c}{2d} \left( l + \frac{1}{\pi} (n + m + 1) \cos^{-1}(\sqrt{g_2}) \right). \quad (2.38)$$

Note that the parameter  $g_2$  can become zero for a plane-plane resonator configuration and negative for a plano-convex cavity. The latter case would not yield any resonant frequencies, because this resonator configuration is unstable as one can easily imagine and verify by looking at the stability diagram in Figure 2.3. For other resonator geometries a more general approach is given in Ref. [11].

The frequency difference between two longitudinal modes ( $n = m = 0$ ) is called the free spectral range (FSR), which is a characteristic number for every cavity that depends only on the cavity length:

$$\text{FSR} = \frac{c}{2d}. \quad (2.39)$$

## 2.6 Light fields in optical resonators

Until now we have only discussed the geometry of cavities and the resulting shape of the beam which is on resonance. Now we should draw our attention towards the light fields themselves and discuss for instance how strong it is and how many round trips it undergoes inside the cavity. Imagining a cavity as depicted in Figure 2.1 with an incident light field  $E_{\text{inc}}$ , one approach to find the reflected light field is to simply sum up its different contributions. These contributions are the light field reflected immediately at the first mirror without entering the cavity, the one doing one round trip and afterward leaves the cavity, the one doing two round trips and so forth:

$$\begin{aligned} E_{\text{ref}} &= -E_{\text{inc}}r + E_{\text{inc}}t^2re^{-i\phi} + E_{\text{inc}}t^2r^3e^{-2i\phi} + \dots \\ &= -E_{\text{inc}}r + E_{\text{inc}}\frac{t^2}{r}\sum_{k=1}^{\infty}(r^2e^{-i\phi})^k \\ &= E_{\text{inc}}\frac{re^{-i\phi} - r}{1 - r^2e^{-i\phi}}, \end{aligned} \quad (2.40)$$

where  $r$  and  $t$  are the field reflection and transmission coefficients of the mirrors. The parameter  $\phi = 2\pi\frac{\nu}{\text{FSR}}$  is the phase shift accumulated in one round trip for light of frequency  $\nu$ , considering only TEM<sub>00</sub> modes. The first minus sign comes from the  $\pi$  phase shift due to the reflection on the back side of the first mirror (see Ref. [10, pp. 35-36] for a derivation of the phase shift). In the last step we used the well known geometric series and assumed lossless mirrors, so that  $|r|^2 + |t|^2 = 1$ . With the same method similar expressions can be found for the light field inside the cavity

$$E_{\text{cav}} = E_{\text{inc}}\frac{t}{1 - r^2e^{-i\phi}} \quad (2.41)$$

and the transmitted light field

$$E_{\text{trans}} = E_{\text{inc}}\frac{t^2e^{-\frac{1}{2}i\phi}}{1 - r^2e^{-i\phi}}. \quad (2.42)$$

The corresponding light intensities can easily be found by the relation

$$\frac{I}{I_{\text{inc}}} = \left| \frac{E}{E_{\text{inc}}} \right|^2, \quad (2.43)$$

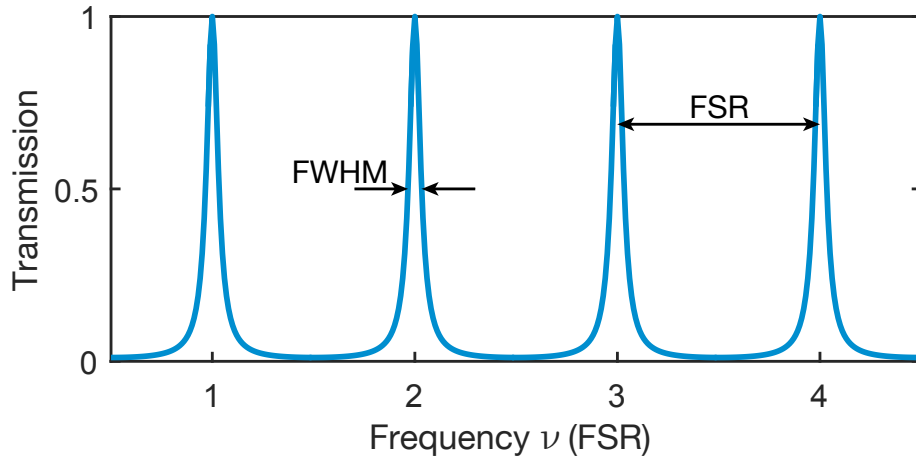


Figure 2.5: Transmitted light intensity of a Fabry-Pérot resonator as a function of the phase accumulated during one round trip. We also indicate the FWHM and the FSR.

which for the transmitted light intensity gives

$$I_{\text{trans}} = I_{\text{inc}} \frac{t^4}{1 - 2r^2 \cos\left(2\pi \frac{\nu}{\text{FSR}}\right) + r^4}. \quad (2.44)$$

Here we have replaced  $\phi$  by  $2\pi \frac{\nu}{\text{FSR}}$  to show the frequency dependence explicitly. Figure 2.6 shows a plot of Eqn. (2.44).

When  $\nu$  fulfills the resonance condition of being a multiple of the FSR, the transmitted intensity has a maximum. In our model the broadness of the peaks depends solely on the reflectivity of the mirrors. After some algebra we find that the half maximum occurs at

$$\nu_{1/2} = \frac{\text{FSR}}{2\pi} \frac{1 - |r|^2}{|r|} \quad (2.45)$$

away from the resonance. A number that is typically used to characterize an optical resonator is the finesse  $\mathcal{F}$  which is defined as the ratio between the free spectral range (FSR) and the full width at half maximum (FWHM)

$$\mathcal{F} = \frac{\text{FSR}}{\text{FWHM}} = \frac{\text{FSR}}{2\nu_{1/2}} = \frac{\pi|r|}{1 - |r|^2} = \frac{\pi\sqrt{R}}{1 - R} \approx \frac{\pi}{1 - R}, \quad (2.46)$$

where  $R = |r|^2$  is the intensity reflection coefficient of each mirror. The last approximation is commonly used for finesse values  $\mathcal{F} > 100$ .

Another useful quantity to describe an optical resonator is the quality factor  $Q$ , which is a measure of the frequency resolution of an optical cavity. Using this definition we can

write  $Q$  as

$$Q = \frac{\nu}{\text{FWHM}}, \quad (2.47)$$

with the resonant frequency  $\nu$ . By using Eqns. (2.46) and (2.39) we can relate  $Q$  to  $\mathcal{F}$  and see that

$$Q = \frac{\nu\mathcal{F}}{\text{FSR}} = \frac{\nu 2d\mathcal{F}}{c} = \frac{2d}{\lambda}\mathcal{F}. \quad (2.48)$$

Here, we replaced the resonant frequency by the resonant wavelength  $\lambda = c/\nu$ . Equation (2.48) states that  $Q$  is equal to the finesse times the number of wavelengths during a full round trip.

## 2.7 Measuring the finesse

Knowledge of the finesse of a cavity is very important, because it determines how narrow the resonances are. As we will see later, the finesse also determines how much we can narrow down the laser linewidth by stabilizing the laser to a high-finesse cavity

Knowing the geometry of the resonator – and therefore the FSR – one simple approach to determine the finesse is to take a tunable laser and slowly scan its frequency over a resonance. With a photo detector we can measure the transmitted intensity on an oscilloscope and read off the FWHM to calculate the finesse. Unfortunately this attempt works only for low finesse cavities, because otherwise the resonances can be far more narrow than the laser linewidth.

To overcome this measurement problem, a better approach is to measure the photon lifetime inside the cavity. If  $U$  is the energy stored inside a cavity, the energy loss will be proportional to the energy  $U$ : on every reflection from one of the cavity mirrors, a fixed fraction of the electric field (and thus the energy) is lost from the cavity. Mathematically we can express the time dynamics with the differential equation

$$\frac{dU(t)}{dt} = -\frac{U(t)}{\tau}. \quad (2.49)$$

Equation (2.49) has a solution

$$U(t) = U_0 e^{-t/\tau}, \quad (2.50)$$

where  $\tau$  is called the intensity ring down time (or photon lifetime). The ring down time  $\tau$  is the characteristic time after which the stored energy has decayed to  $1/e$  times its original value. While traveling one cavity length  $d$ , the energy decay of the light field in our absorption free cavity is equivalent to  $1 - R$ . Per unit time this would be  $\frac{c}{d}(1 - R)$  so we can write

$$\frac{dU(t)}{dt} = -\frac{c}{d}(1 - R)U(t) \quad (2.51)$$

and find

$$\frac{1}{\tau} = \frac{c}{d}(1 - R). \quad (2.52)$$

Using Eqn. (2.52) together with the approximation in Eqn. (2.46) we can finally connect the finesse to the ring down time:

$$\mathcal{F} = \frac{c\pi\tau}{d}. \quad (2.53)$$

Equipped with Eqn. (2.53) it is possible to obtain the finesse by a simple ring down time measurement. To do so, a laser needs to be stabilized onto one of the resonances of the corresponding cavity and at one point it must be switched off very rapidly. As shutting down the laser or simply blocking the beam is not a fast enough way to do this, we used an acousto-optic modulator (AOM). The basics of AOMs are well described in Ref. [16]. Here, we can look at an AOM as a device that uses sound waves traveling through a crystal. Those sound waves (phonons) form a crest that can diffract light of a laser beam. The diffracted beam leaves the AOM in an angle and can be isolated from the undiffracted beam. We can stabilize the diffracted beam on a cavity and shut down the AOM (and therefore the diffracted beam) within nanoseconds. The result of such a measurement can be seen in Figure 2.7.

This method is very straightforward and easy to evaluate, but to perform it a laser has to be stabilized onto a cavity resonance. Stabilizing a laser onto a high finesse cavity is usually quite time consuming, so it would be great to have a method to determine the finesse without having to lock a laser to the cavity. An alternative approach is to scan the laser quickly over a cavity resonance. When the ring down time of the cavity becomes comparable to the time it takes the laser to sweep over the resonance, interference effects in the transmitted and reflected light signal become visible. Photons that enter the cavity at a certain time will do a round trip and then interfere with the photons entering the cavity after this round trip, which are now shifted in frequency due to the scan. The resulting signal might appear difficult to evaluate, but summing the different contributions up [17], we find that the dynamics of the intracavity field are governed by a first order differential equation

$$\frac{dE_{\text{cav}}}{dt'} = -(1 - i\tilde{\nu}t')E_{\text{cav}} + i\frac{\sqrt{T}\mathcal{F}}{\pi}E_{\text{inc}}. \quad (2.54)$$

Here,  $t' = t/(2\tau)$  is the time normalized to twice the intensity ring down time and

$$\tilde{\nu} = \frac{4\mathcal{F}d\dot{\omega}\tau}{\pi c} \quad (2.55)$$

is the normalized scan rate, with the scan rate  $\dot{\omega}$  of the laser frequency in rad/s<sup>2</sup>. Equation (2.54) can be used to find solutions for the transmitted and reflected signal of a cavity

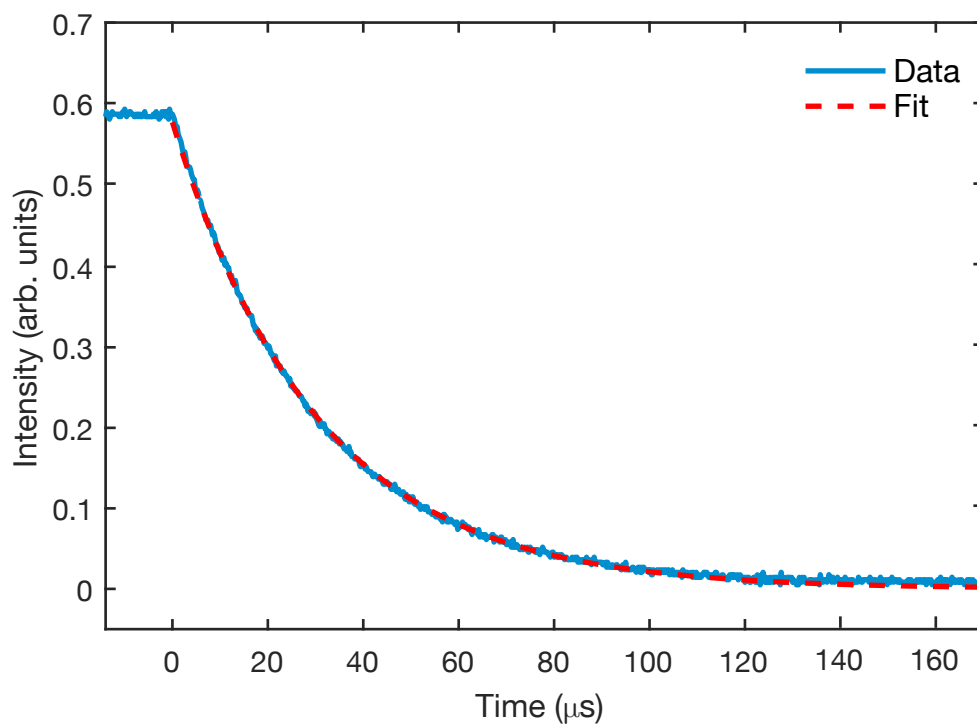


Figure 2.6: A ring-down measurement of the intensity stored inside an optical cavity. The measured data (blue line) and the fit (red line) agree perfectly and reveal a ring down time of  $30.3(1) \mu\text{s}$ . The cavity is 10 cm long cavity, so this ring down time corresponds to a finesse of 286 000.

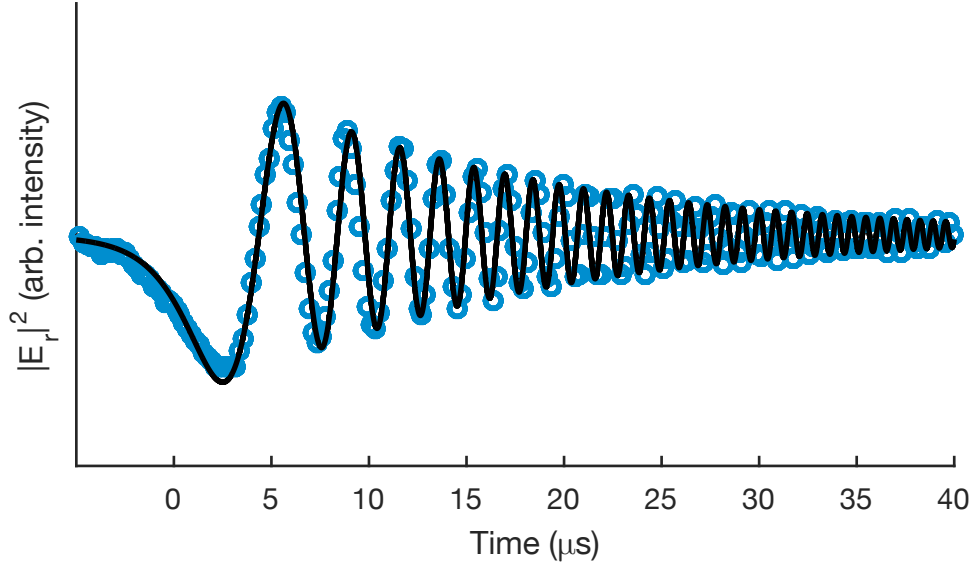


Figure 2.7: Fitted reflection signal while scanning over a resonance of an optical cavity. The fit agrees very good with the measured data and reveals a ring down time of  $7.4(5) \mu\text{s}$ . The resulting finesse is 69 000 for a 10 cm long cavity.

while scanning over a resonance. We find [18]

$$|E_{\text{ref}}(t)|^2 = |E_{\text{inc}}| \left| 1 - \frac{\beta}{\tilde{\nu}} \left[ \sqrt{\frac{\pi}{2i}} e^{-t' + i\tilde{\nu}t'^2/2 - i/(2\tilde{\nu})} + \sqrt{2i} D\left(\frac{i + t'\tilde{\nu}}{\sqrt{2i\tilde{\nu}}}\right) \right] \right|^2 \quad (2.56)$$

and

$$|E_{\text{trans}}(t)|^2 = \frac{\beta^2 |E_{\text{inc}}|}{\tilde{\nu}} \left| \sqrt{\frac{\pi}{2}} e^{-t' + i\tilde{\nu}t'^2/2 - i/(2\tilde{\nu})} + i\sqrt{2} D\left(\frac{i + t'\tilde{\nu}}{\sqrt{2i\tilde{\nu}}}\right) \right|^2, \quad (2.57)$$

where  $\beta = T/(1 - R)$  is the cavity contrast parameter and  $D(x)$  is the Dawson integral. Equations (2.56) and (2.57) can be fitted to a measurement. Figure 2.7 shows such a measurement and the result of a fit. To fit such a highly non linear equation might seem to be challenging, but closer examination reveals that the exponential decay of the function depends only on the ring down time  $\tau$  and the oscillation frequency of the intensity depends only on the scan rate  $\dot{\omega}$ . The measured amplitude depends on the photo detector gain and the laser power and therefore it is enough to determine it once and use the same value also for further measurements. With  $\tau$  and Eqn. (2.53) it is possible to determine the finesse.

Measuring the finesse accurately can be very important to determine the performance of an optical resonator. In our case it was the first indication that the mirrors of our resonator were contaminated, because we measured a finesse of only 69 000 (Fig. 2.7) although the supplier specified more than 200 000. After the mirrors were replaced we measured a linewidth of 286 000 (Fig. 2.7), which was sufficient to proceed with the experiment.

# Chapter 3

## Laser stabilization

By laser stabilization we mean the process of stabilizing the laser light frequency. Lasers are a monochromatic source of coherent light, but looking more closely we will see that being monochromatic is only partially true. In practice frequency fluctuations lead the laser to emit a range of frequencies around their central frequency, which motivates the introduction of the linewidth of a laser. The linewidth can be obtained by measuring the instantaneous laser frequency over a certain time interval  $\Delta t$ , plotting a histogram and calling its FWHM the linewidth. This definition of the linewidth might cause confusion, because how much the emitted frequency can change depends on  $\Delta t$  making the measured linewidth a function of  $\Delta t$ . Therefore it is worthwhile to clarify the terminology before beginning, and here I will follow the definitions given in Ref. [19]:

- The fast linewidth (or simply linewidth) corresponds to a  $\Delta t$  of  $10^{-5}$ - $10^{-4}$  s, which is less than typical spectroscopic interaction times. Therefore the fast linewidth sets a limit on the smallest feature the laser can still resolve.
- Lower frequency fluctuations can cause the fast linewidth to jitter along the frequency axis. Jitter can be caused for example by vibrations that typically lie in the kHz region.
- Even slower changes of large amplitude can be caused for instance by temperature fluctuations. One says that the frequency of the laser “drifts”.

Bearing these definitions in mind, we can already conclude what our laser stabilization scheme should be capable of achieving: we want it to prevent our laser from drifting over time and it should reduce frequency fluctuations to narrow down the linewidth of the laser. Furthermore it should be very stable against vibrations that could be present on the optical table where the laser is located. To achieve this performance we have to cover a large frequency range. To learn how we can achieve this stabilization we will first have a look at feedback and control theory, which tells us how a physical quantity can be stabilized to a certain value. For stabilization we need to measure deviations from this value very precisely. For laser frequency stabilization, the so called Pound-Drever-Hall

(PDH) scheme provides this precision, by comparing the laser frequency to a resonance of an optical resonator used as a frequency reference.

### 3.1 Feedback and control theory

Very often it happens that one wants to set a physical quantity to a certain value at which it should remain without fluctuations. Such a quantity might be the velocity for cruise control in a car, the temperature in a room or even the pupil radius to control the amount of light that reaches the retina in our eyes. How to achieve this performance is the subject of control theory.

We want to confine our attention to simple systems, which have one input parameter  $u$  and one output parameter  $y$ . In control theory, the signal flow is often depicted by block diagrams where each system is represented as a block. An example is shown in Figure 3.1, where a signal  $u(s)$  with complex frequency  $s$  serves as input signal for a system (gray box). The system then transforms the input into the output  $y(s)$ . We can assign a transfer function  $G(s)$  to the system, which is the ratio between the input and the output signal:

$$G(s) \equiv \frac{y(s)}{u(s)}. \quad (3.1)$$

The definition of the transfer function in Eqn. (3.1) motivates the representation of signal flow in block diagrams, because now the output signal  $y$  can simply be calculated by multiplying the transfer function to the input signal. More complicated diagrams can involve several systems with different transfer functions. The total transfer function is then obtained by multiplying the transfer function of each single system.

Notice that the discussion up to here has taken place in the frequency domain. In control theory it is often more practical to work with signals of fixed frequencies instead of time dependent signals. These two representations are connected through the one-sided Laplace transform, which is a generalization of the Fourier transform to complex frequencies  $s$ . The Laplace transform of a function  $f(t)$  is

$$\mathcal{L}[f(t)] \equiv f(s) = \int_0^{\infty} f(t)e^{-st} dt. \quad (3.2)$$

With this definition, important relations that we will use in the following are [20]:

$$\mathcal{L}[d^n f(t)/dt^n] = s^n f(s) \quad \text{and} \quad (3.3)$$

$$\mathcal{L}\left[\int f(t)dt\right] = f(s)/s. \quad (3.4)$$

A more detailed discussion about Laplace transform and its applications in control theory can be found in Ref. [21].

Now we will try to “control” the output  $y$  of the system  $G$  and set it to the desired value. One approach is to measure the output signal. From this measurement we can infer how far we are from the desired set point and use this information to apply an appropriate input  $u$ . With this method we feed the output  $y$  back into the input  $u$ .



Figure 3.1: This simple block diagram illustrates an input signal  $u(s)$  to a system  $G$  and its output signal  $y(s)$ .

### 3.1.1 Feedback

The idea of feedback is to force an output  $y(t)$  of a system to track a set point or reference signal  $r(t)$  as closely as possible. To understand how this tracking is accomplished, we consider a system with transfer function  $G$ . The general approach is to measure the output  $y(t)$  of the system and compare it to the reference signal  $r(t)$ . The difference between the measured output and the reference is called error signal

$$e(t) \equiv r(t) - y(t). \quad (3.5)$$

Ideally, we can use the error signal together with a control system  $K$  to calculate the appropriate input signal  $u(t)$  such that the output of  $G$  follows the reference. For a block diagram representation of this feedback see Figure 3.2, where the derivation of the error signal is indicated by the plus and minus sign.

From the block diagram in Figure 3.2 we can read off how the error signal relates to the system's output

$$y(s) = G(s)K(s)e(s). \quad (3.6)$$

Using Eqn. (3.5) we can also find the relation between the output and the reference

$$y(s) = \frac{G(s)K(s)}{1 + G(s)K(s)}r(s). \quad (3.7)$$

When feeding the output back into the input, one says that one closes the loop. The factor in front of  $r(s)$  in Eqn. (3.7) is called the closed loop gain. When interrupting the feedback loop at any point we would be left with the open loop gain  $G(s)K(s)$ .

Equation (3.7) suggest that we can choose a control law  $K$  to “shape” the system dynamics, such that the new overall transfer function

$$T = \frac{G(s)K(s)}{1 + G(s)K(s)} \quad (3.8)$$

has the dynamics that we want. And indeed, for many systems you can find a suitable  $K$ . In Ref. [22] John Bechoefer provides a great collection and practical examples of how feedback can improve the systems dynamics.

### 3.1.2 Examples for control laws

The probably most intuitive form of  $K(t)$  is proportional feedback. Proportional feedback means that the error signal amplified with a constant is fed back into the controller, so  $u_p(t) = k_p e(t)$  where  $k_p > 0$ . With the definition of the error signal in eqn. (3.5),  $e$  is negative when the output  $y$  is above the reference  $r$  and positive as soon as it falls below  $r$ . The proportional feedback tends to counteract disturbances and can therefore have a stabilizing effect.

Using only the proportional gain has the disadvantage that the control signal becomes zero as  $y$  approaches  $r$ . As a result, the input  $u$  becomes zero as well and the system will start to drift away from the reference point. We can solve this problem by applying an integral control, such that the input becomes

$$u_i(t) = k_i \int_{-\infty}^t e(t') dt'. \quad (3.9)$$

Here  $k_i$  is the integral gain. With the integral control the control signal becomes a function of the history of the error signal and thus it provides a control signal although the error signal is zero. Laplace transforming Eqn. (3.9) with Eqn. (3.3) we find that the integral control law is

$$\frac{u_i(s)}{e(s)} = K_i(s) = \frac{k_i}{s}. \quad (3.10)$$

We see that the integral control has high gain for low frequencies which rolls off at high frequencies. A control system with this behavior is called an integrator.

Another commonly used controller is derivative feedback. A derivative feedback controller calculates the input by

$$u_d(t) = k_d \dot{e}(t), \quad (3.11)$$

with the derivative gain  $k_d$ . The derivative control predicts the future development of  $e(t)$  and tries to counteract disturbances before they occur. Looking at the Laplace transform of Eqn. (3.11) using Eqn. (3.4)

$$K_d(s) = k_d s, \quad (3.12)$$

we see that the differentiator has high gain for high frequencies and therefore rejects fast changing signals very well. It is often used to extend the feedback bandwidth of a control system.

A combination of these three control laws results in the famous proportional-integral-derivative controller (PID controller). The PID controller is very common and can be applied to various systems. In this thesis we used it for instance to control the temperature of the frequency reference in Chapter 4 and the temperature of the home-built laser discussed in Chapter 6.

We have seen that all these ideas require a precise knowledge of the error function. Inferring this information is not always easy. The next section will discuss how an error signal can be obtained for controlling a laser frequency.

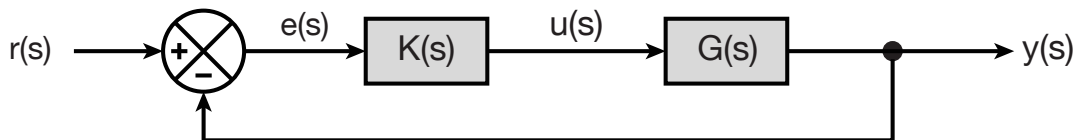


Figure 3.2: Block diagram representation of a feedback control loop. The error signal  $e$  is calculated according to Eqn. (3.5), illustrated by the plus and minus sign in the comparator. The error signal is then fed into a controller  $K$  that transforms  $e$  into an input  $u$ .

## 3.2 PDH locking

To stabilize the frequency of the laser light we will have to measure frequency deviations of the laser very accurately and quickly. The frequency of visible light is in the range of several hundred THz and with today’s electronics it is not possible to resolve the oscillations of the electric field directly. Therefore our strategy will be to take a reference, of which we know the frequency very precisely and “lock” our laser to this reference. As we have seen in the preceding chapter, an optical resonator could provide us with such a reference: The transmission signal of an optical resonator in Figure 2.6 shows that the resonator only transmits light of certain frequencies that are close to the resonance frequency. For high finesse resonators the resonances can be very narrow. For instance a 10 cm long resonator with a finesse  $\mathcal{F} = 280\,000$  has a FWHM of only 5.4 kHz and would serve as a very good reference.

Given a laser one wants to stabilize, we could imagine to simply tune the frequency of the laser to one of the resonances and watch the transmission signal on a photo detector (PD). A drift in frequency of the laser is then recognized by a decreasing signal on the PD and we could use this information to correct the frequency again.

Unfortunately in reality this very simple approach does not work for several reasons: first the PD cannot distinguish between a varying light intensity due to frequency change or intensity modulation of the laser itself. Even more severe is the symmetry of the transmission peak of an optical resonator. By only looking at the transmission signal we can not tell in which direction the frequency is changing. Both issues can be resolved by using the Pound-Drever-Hall locking scheme for frequency stabilization, which will be discussed in this section. A very good introduction to PDH locking can be found in Ref. [23].

To overcome the problem of intensity fluctuations caused by the laser, we can use the reflected light signal instead of the transmitted light signal. At resonance, the reflection signal is zero, independent of the incident laser power. Thus frequency and intensity noise get decoupled. The symmetry problem remains, as the reflected light signal is also symmetric around the resonance. To find a workaround, we have to study the reflected light signal closer. We assign a transfer function to the cavity which relates the reflected light field to the incident light field. We obtain the reflection coefficient by dividing the

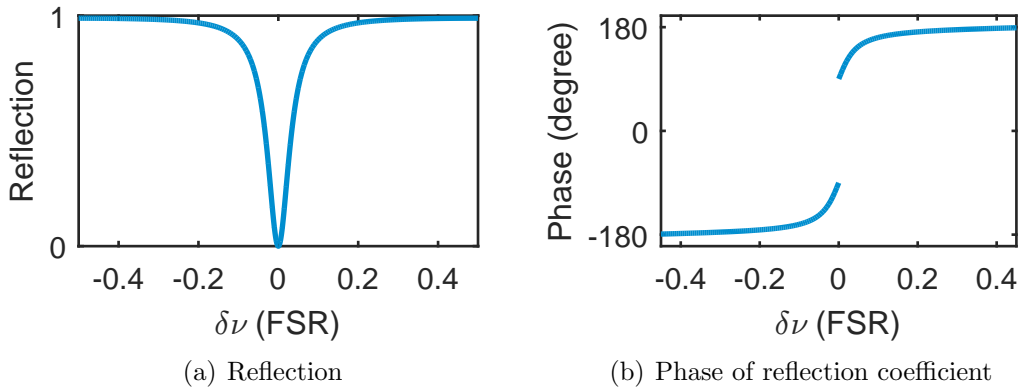


Figure 3.3: Plots of (a) the magnitude-squared of the reflection coefficient, giving the cavity reflection and (b) the phase of the reflection coefficient. The figures are plotted with a reflectivity  $r = 0.9$ .

reflected light field in Eqn. (2.40) through the incident light field  $E_{\text{inc}}$

$$R(\omega) = \frac{E_{\text{ref}}}{E_{\text{inc}}} = \frac{r \left( \exp \left( i \frac{\omega}{\text{FSR}} - 1 \right) \right)}{1 - r^2 \exp \left( i \frac{\omega}{\text{FSR}} \right)}, \quad (3.13)$$

where  $\omega = 2\pi\nu$  is the angular frequency, corresponding to the laser frequency  $\nu$ . This complex number has an amplitude  $|R(\omega)|$  equal to the amount of reflected light in units of  $E_{\text{inc}}$  and a phase  $\arg[R(\omega)]$  which is the phase shift the reflected light field undergoes upon reflection. Plotting  $|R(\omega)|^2$  and  $\arg[R(\omega)]$  in Figure 3.3 reveals that this phase of the reflected light is not symmetric around a resonance. If we are able to measure the phase, we know if the laser frequency increases or decreases.

The PDH-locking scheme is meant to perform exactly this measurement. The basic setup to perform PDH-locking for a diode laser is depicted in Figure 3.4. The diode laser emits light of frequency  $\omega$  and field amplitude  $E_0$ . To isolate the reflected signal from the cavity we use a quarter wave plate and polarizing beam splitter (PBS). The initially p-polarized beam crosses the PBS without being affected. Passing the quarter wave plate twice transforms the beam into the s-polarized state, which is reflected at the PBS, and can be measured with a photo detector. Before reaching the cavity, the beam is phase modulated by an electro optical modulator (EOM). The topics of EOM are well described in Ref. [24]. An EOM is an optical device that can shift the phase of electromagnetic radiation proportional to an applied voltage. In this example a local oscillator provides a sinusoidal voltage signal of frequency  $\Omega$  that drives the EOM. The light passing through the EOM becomes

$$E_{\text{inc}} = E_0 e^{i(\omega t + \beta \sin \Omega t)}. \quad (3.14)$$

Here,  $\beta$  is the modulation depth which is proportional to the amplitude of the applied voltage signal. Equation (3.14) can be expanded using Bessel functions [23]

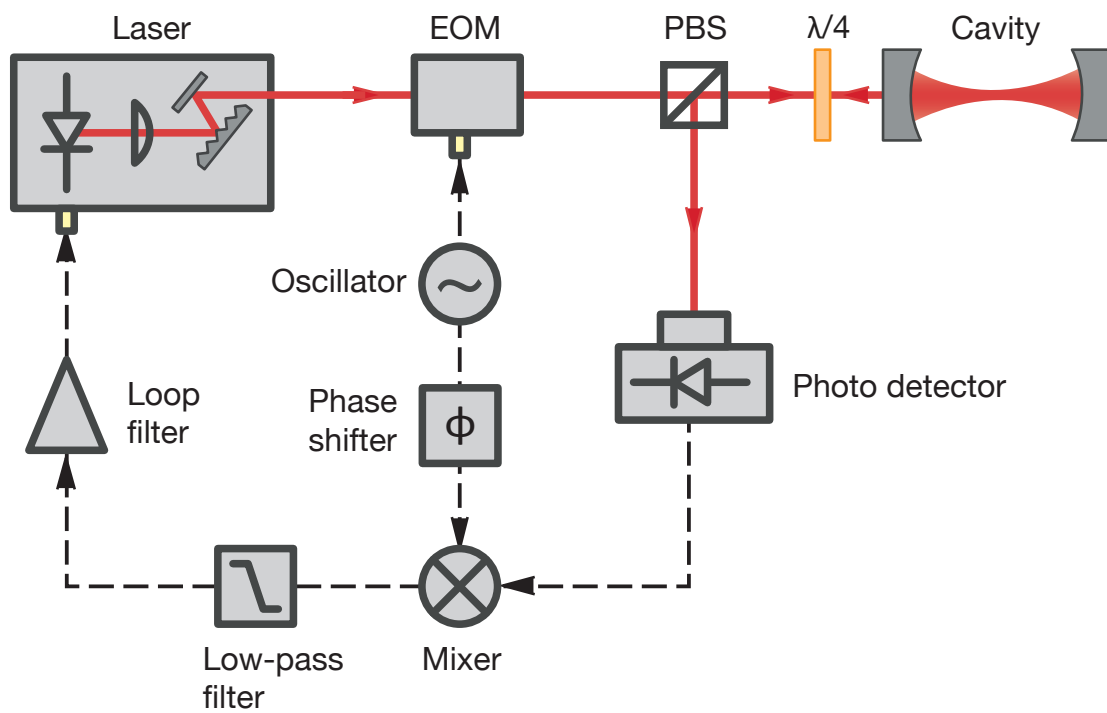


Figure 3.4: Schematic setup for the Pound-Drever-Hall locking scheme. Light rays are indicated by the red lines and the electrical signal flow is indicated by the dashed black lines.

$$\begin{aligned}
E_{\text{inc}} &\approx [J_0(\beta) + 2iJ_1(\beta) \sin \Omega t] e^{i\omega t} \\
&= E_0 [J_0(\beta) e^{i\omega t} + J_1(\beta) e^{i(\omega+\Omega)t} - J_1(\beta) e^{i(\omega-\Omega)t}].
\end{aligned} \tag{3.15}$$

Equation (3.15) gives rise to a very intuitive way to explain the effect of the EOM with a sinusoidal signal. We have three beams incident on the cavity with three different frequencies: the carrier with unchanged frequency  $\omega$  and intensity  $I_c = J_0^2(\beta)I_0$  and two sidebands with frequencies  $\omega \pm \Omega$  and intensities  $I_s = J_1^2(\beta)I_0$ . We can apply the reflection coefficient in Eqn. (3.13) to each of the three beams at the corresponding frequency to derive the electric field of the reflected beam:

$$E_{\text{ref}} = E_0 [R(\omega)J_0(\beta)e^{i\omega t} + R(\omega + \Omega)J_1(\beta)e^{i(\omega+\Omega)t} - R(\omega - \Omega)J_1(\beta)e^{i(\omega-\Omega)t}]. \tag{3.16}$$

The phase information we are interested in is entered through the reflection coefficient in Eqn. (3.16). One can already guess the intention behind this procedure: the oscillation of the electric field is far too fast to be observed directly with any electrical device. Therefore we created two extra beams with different frequencies but a definite phase relation. By overlapping these beams, their individual electric fields will interfere with each other and create an oscillating envelope. One speaks of a beat signal with a frequency equal to the frequency difference of the interfering beams. In our case the beat frequency is  $\Omega$ , which typically has a MHz frequency. Hence, this frequency is far lower than the optical frequency and the beating signal's phase can be resolved with a fast photo detector. We should keep in mind that the photo detector does not measure the electric field, but the light intensity. We use Eqn. (2.43) to calculate the intensity on the photo detector [23]

$$\begin{aligned}
I_{\text{ref}} &= I_c |R(\omega)|^2 + I_s \{ |R(\omega + \Omega)|^2 |R(\omega - \Omega)|^2 \} \\
&\quad + 2\sqrt{I_c I_s} \text{Im}[R(\omega)R^*(\omega + \Omega) - R^*(\omega)R(\omega - \Omega) \sin(\Omega t) \\
&\quad + (2\Omega \text{ terms})],
\end{aligned} \tag{3.17}$$

where we assume that the modulation frequency is far higher than linewidth of the cavity, i.e.  $\Omega \gg \text{FSR}/\mathcal{F}$ . In Eqn. (3.17) the first line contains oscillations with the light frequency  $\omega$ , which averages out to a DC signal on the PD. The second line includes the desired beating signal between the carrier and the sidebands and the third line represents the beating signal of the two sidebands against each other with frequency  $2\Omega$ . The electric signal

$$U(\omega) = U_{\text{DC}} + e(\omega) \sin(\Omega t) + (2\Omega \text{ terms}), \tag{3.18}$$

of the PD is proportional to  $I_{\text{ref}}$ , with the PDH error signal

$$e(\omega) \propto \text{Im}[R(\omega)R^*(\omega + \Omega) - R^*(\omega)R(\omega - \Omega)]. \tag{3.19}$$

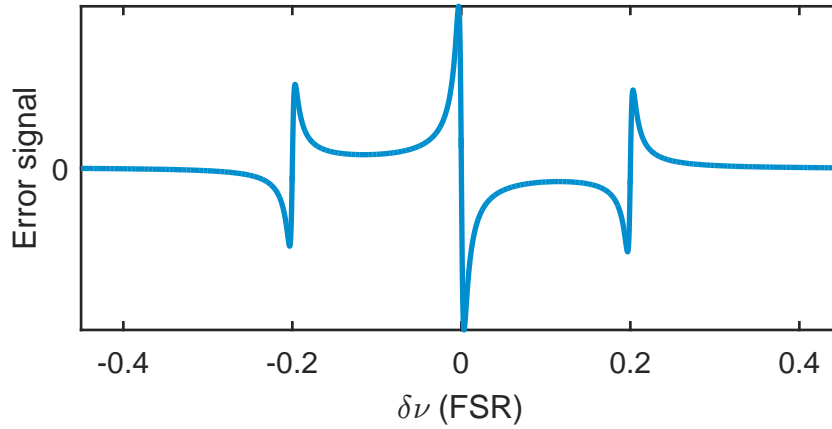


Figure 3.5: Schematic setup for the Pound-Drever-Hall locking scheme. Light rays are indicated by the red lines and the electrical signal flow is indicated by the dashed black lines.

We isolate the error signal by comparing it with the signal of the local oscillator. This operation is done via a frequency mixer, which performs the mathematical operation of multiplying its inputs. With the mathematical identity

$$\sin(\alpha x) \sin(\alpha' x) = \frac{1}{2} \{ \cos[(\alpha - \alpha')t] - \cos[(\alpha + \alpha')t] \} \quad (3.20)$$

we see that the multiplier output will be equal to

$$\begin{aligned} U_{\text{mult,out}} &= [U_{\text{DC}} + e(\omega) \sin(\Omega t)] \times \sin(\Omega t) \\ &= \frac{1}{2} e(\omega) + U_{\text{DC}} \sin(\Omega t) - \frac{1}{2} e(\omega) \cos(2\Omega t). \end{aligned} \quad (3.21)$$

The following low pass filter gets rid of the remaining oscillating terms in (3.21) and we are left with the error signal, which is plotted in Figure 3.5.



# Chapter 4

## Ultrastable reference cavity

An ultrastable reference cavity system consists of two parts: the reference cavity and the cavity housing. The purpose of an ultrastable reference cavity housing is to provide an environment which is extremely well isolated from the outside world. State-of-the-art cavity housing designs even allow transporting the reference cavity in a car [25].

When I joined the lab, I took over the project from the former master student Nejc Janša to construct such an ultrastable reference cavity. In his master thesis [26], he thoroughly describes and justifies the design of the ultrastable reference cavity housing as well as reports on the first progress to assemble the cavity housing.

This chapter briefly reviews the important concepts of what needs to be considered when building a stable frequency reference system. Then, we focus on how the whole system was assembled and the problems we encountered. To conclude we discuss the measurements that were performed to test the cavity's isolation from external temperature fluctuations.

### 4.1 Frequency stability of a resonator

The resonant frequencies of an optical resonator and its stability can be influenced by several effects. Light is resonant with a cavity of length  $d$ , if its frequency  $\nu$  is a multiple of the free spectral range of the cavity:

$$\nu = \frac{lc}{2dn}. \quad (4.1)$$

Here,  $l$  denotes the longitudinal mode number,  $c$  is the speed of light in vacuum, and  $n$  is the index of refraction of the material inside the resonator. From Eqn. (4.1), we can see that the resonant frequencies depend only on two quantities that might be subject to variations: the cavity length  $d$  and the index of refraction  $n$ . To see how changes in  $d$  or  $n$  affect  $\nu$ , we take the total derivative of Eqn. (4.1) and divide the result through Eqn. (4.1). We find an expression for the fractional stability of  $\nu$  which depends on both the

fractional stability of the cavity length and the fractional stability of the refractive index:

$$\frac{\Delta\nu}{\nu} = -\frac{\Delta d}{d} - \frac{\Delta n}{n}. \quad (4.2)$$

Focusing on changes in the cavity length we can conclude that we need a length stability in the  $10^{-16}$  m range for a frequency stability of 1 Hz. This means that the length stability has to be on the order of the proton radius. One can imagine that from a technical point of view, achieving such length stabilities is a challenging task.

### 4.1.1 Thermal expansion

Most materials expand (contract) under the influence of rising (falling) temperature  $T$ . Changes in the temperature are connected to length changes as

$$\frac{\Delta d}{d} = \alpha(T) \Delta T + \frac{1}{2} \alpha'(T) \Delta T^2 + \mathcal{O}(\Delta T^3), \quad (4.3)$$

where  $\alpha$  is the coefficient of linear thermal expansion (CTE),  $\alpha'(T)$  is its first derivative with respect to  $T$ , and  $\frac{\Delta d}{d}$  is the fractional length change that occurs when the temperature is changed by  $\Delta T$ . To hold  $d$  as constant as possible, one usually attaches the mirrors of a cavity to a “spacer” which holds the mirrors at a constant distance. Ideally, the spacer material has a very low CTE. Table 4.1 lists the most common spacer materials and their values for their CTE; we see that ULE-glass and ZERODUR are good candidates as spacer materials.

Material	$\alpha_T$ in $\text{K}^{-1}$	$E$ in GPa
Corning ULE <sup>®</sup> -glass Premium Grade	$0 \pm 30 \times 10^{-9}$	67.6
ZERODUR <sup>®</sup> Expansion Class 2	$0 \pm 100 \times 10^{-9}$	90.3
Fused Silica	$5 \times 10^{-7}$	72
Copper	$17 \times 10^{-6}$	127

Table 4.1: A list of common spacer materials with their CTE at room temperature and Young’s modulus. Copper is listed for comparison. Values are taken from Refs. [27], [28], [29] and [30], respectively.

The CTE itself is also a function of temperature, and for certain materials, there is a temperature at which its first order contribution vanishes, i.e.  $\alpha(T) = 0$ . To minimize the effects of temperature changes further, spacers can be operated at this zero-crossing temperature. Taking  $\alpha'(T) = 1.7 \times 10^{-9} \text{K}^{-1}$  [18] in the case of ULE-glass near its zero-crossing, we see that fractional length changes in the  $10^{-15}$  range require a temperature stability of less than 1 mK.

Furthermore, to minimize the effects of thermal expansion, one must find a good way to support the resonator. If the cavity is sitting on a material with a very different CTE, temperature fluctuations might induce stress, bend the spacer and therefore alter the cavity

length. The proper method is to decouple the spacer with an elastic material and let the spacer sit on another construction with low expansion glass, for instance Zerodur.

### 4.1.2 Vibrations

Another natural reason for changes in the cavity length are vibrations, which bend and deform the spacer. The total length change  $\Delta d$  of a material which is exposed to an external force  $F$  is determined by its Young's modulus

$$E = \frac{Fd}{A\Delta d}. \quad (4.4)$$

Here,  $F$  is applied to a surface  $A$  of an object with length  $d$ . Although we are already quite limited in our choice of materials with a low CTE, one might try to maximize Young's modulus or choose a spacer with a large cross-section. This method can improve the performance by a small factor. However, to make the system nearly insensitive to vibrations one has to apply different methods.

A great way to reduce the sensitivity of the cavity length to vibrations by orders of magnitude is to support the optical resonator in a way such that length changes caused by vibrations cancel out and conserve the total length of the cavity. These special supporting points can be found via finite element analysis as described in Ref. [31] and should be considered when designing the cavity housing.

Another possibility to decouple the cavity from vibrations is to use a vibration isolation platform. Recent progress in precision optics experiments like gravity wave detectors have improved the technique of vibration isolation tremendously (see for example Ref. [32] for a state of the art vibration isolation platform). Commercial vibration isolation platforms are available in active and passive versions and in a large variety of different sizes. Furthermore, one might consider to choose an elastic material as supporting pads for the cavity. These materials can absorb vibrations effectively, especially if the vibrations have to go through several layers. To account for acoustical noise one can build an acoustical shield around the cavity system.

### 4.1.3 Pressure fluctuations

Equation (4.2) shows that not only changes in the spatial cavity length are of importance. The optical path length is the important quantity that has to be kept constant. Pressure fluctuations alter the refractive index of the medium between the cavity mirrors, and therefore, change the optical path that a light ray traverses. At a pressure of one atmosphere, air has a refractive index of  $n_{air} = 1.0003$  and vacuum has  $n_{vac} = 1$  by definition. Assuming a linear dependence, these two numbers can be interpolated to obtain the refractive index as a function of the pressure  $p$

$$n(p) \approx 1 + \frac{3 \times 10^{-7}}{\text{mbar}} p. \quad (4.5)$$

This rough estimate, Eqn. (4.2) and the assumption that the absolute pressure  $p \ll 1$  mbar can be used to estimate the effect of pressure fluctuations on the frequency stability:

$$\frac{\Delta\nu}{\nu} \approx -\frac{3 \times 10^{-7}}{\text{mbar}} \Delta p. \quad (4.6)$$

From Eqn. (4.6), we can conclude that we need a pressure stability of at least  $10^{-8}$  mbar to keep the effects on the frequency stability in the  $10^{-15}$  range. Therefore, it is necessary to store the cavity in vacuum. Storing the cavity in vacuum has further advantages: for instance, thermal heat conduction by convection is suppressed and acoustic phonons cannot propagate through the vacuum.

## 4.2 Design

Choosing a good design for the cavity housing is very important, because the design determines how well the reference cavity can be decoupled from environmental disturbances. The final design was done by Nejc Janša, and the design includes elements from commercial systems and from the “JILA cavity” in Ref. [18]. Figure 4.1 shows a picture of the completely assembled cavity system. On the picture, the chamber is located on the edge of the optical table for alignment purposes. Later, the setup will be moved to the table center as the center position is the least effected by vibrations. This section briefly describes the design of the stable reference cavity. For details, see Ref. [26]. To do so, we start at the bottom and work through the different elements towards the optical resonator. In Figure 4.2 you can see a rendering of the chamber with its different sections.

### 4.2.1 The chamber

The whole vacuum chamber sits on a vibration isolation stage that was bought from MinusK Technology. The stage is completely passive and it features very low natural frequencies, which are 0.5 Hz vertically and 1.5 Hz horizontally. The custom-cut breadboard provides a surface to mount the required optics and lies on four Sorbothane pads, which further dampen vibrations. The breadboard is cut in a way that fits exactly on the vibration isolation stage and still allows access to the shipping screws, which are useful to lock the vibration isolation stage when mounting optics.

The main vacuum chamber is made out of aluminum, alloy EN AW 5083. Although the best vacuum results are achieved with stainless steel, its thermal conductivity  $\kappa$  is rather low compared to aluminum (see Table 4.2). A high thermal conductivity is required to ensure fast temperature homogenization around the chamber. Together with the high heat capacity of aluminum, the chamber acts as a passive low pass filter for temperature variations.

In the front two electrical feedthroughs are realized as D-sub 9 connectors and the two windows on the right and left-hand sides provide optical access to the cavity. The windows are tilted to avoid any undesired back reflection. One of the downsides of aluminum is that

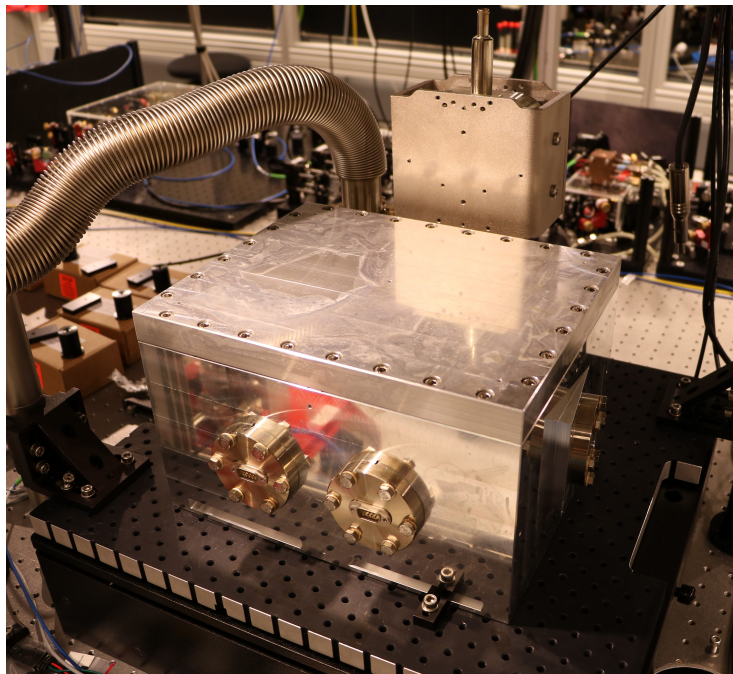


Figure 4.1: Vacuum housing of the reference cavity. The aluminum vacuum chamber sits on the black vibration isolation stage, separated by a breadboard which later is used to mount all the necessary optics. On the back side one sees the ion pump that is connected through a 5-way cross to the chamber. An angle wave is connected to another port of the 5-way cross, which allows to connect a turbo pump via a flexible bellow (top left).

aluminum is a very soft metal, and therefore you cannot use copper gaskets for sealing any of these conflat connections. Alternative gaskets are made out of Viton. Viton is good for high vacuum applications and can be used inside the chamber as well. Unfortunately, Viton is penetrable for noble gases which limits our vacuum and has to be considered when choosing the vacuum pump.

On the back side of the chamber, a 5-way cross connects an “easy close” angle valve and an ion pump to the chamber. The ion pump provides a vibration free possibility to keep the pressure in the chamber continuously low once the chamber was pumped out with the membrane and turbo pumps. We used a 10SW DI ion pump from Gamma Vacuum with a pumping speed of 8 L/s. It is important that this pump is able to pump noble gases, as they might penetrate through the Viton seals.

Material	$\kappa \left( \frac{\text{W}}{\text{mK}} \right)$	$c \left( \frac{\text{J}}{\text{kgK}} \right)$
Stainless Steel	16.2	500
Aluminum EN AW 5083	120	900
Copper EN CW008A	393	385

Table 4.2: A list of commonly used materials for vacuum technology. We compare their thermal conductivities  $\kappa$  and specific heat capacities  $c$ . Although best vacuum results are achieved with stainless steel, its thermal conductivity is rather low.

### 4.2.2 Active temperature stabilization

Inside the aluminum vacuum chamber sits a box made of copper. This box is actively temperature stabilized and copper with its high thermal conductivity is perfectly suited for this purpose. To use copper inside high vacuum, we have to be careful which alloy of copper we use. For this box we decided on the alloy EN CW009A, which has a very low oxygen content. The shield is made out of eight parts, which have very flat contact surfaces and are carefully screwed together to have the best possible thermal contact between them. The copper box sits on four Viton pads. To reference the box to outer chamber, both the bottom of the aluminum chamber and the bottom part of the copper box have square extrusions that fit to the Viton pads. These extrusions have small spiral extrusions that should prevent air from getting stuck below the Viton pads. This should prevent virtual leaks that contaminate the vacuum. For the same reason every thread has a venting hole to not allow air to get stuck between thread and screw.

To temperature stabilize the copper box Kapton heating tapes are used. They are compatible with in-vacuum use and come in various shapes and power specifications. In total four heating tapes are glued onto the copper box, one on each of the larger sides. The copper box features small holes on each of its sides to glue thermistors with good thermal contact into them. These thermistors are used to control the heating elements and to monitor the temperature of the box.

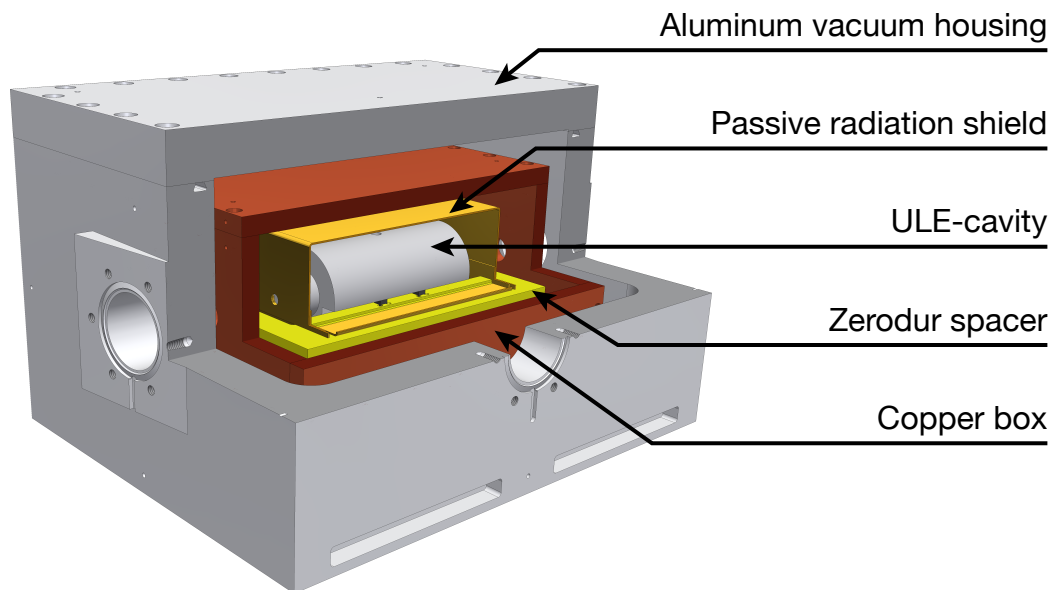


Figure 4.2: This rendering shows the different stages of the cavity housing. Going from outside to the inside you see the aluminum vacuum chamber, the temperature controlled copper box, the passive radiation shield and the ULE-cavity, which sits on a Zerodur spacer.

### 4.2.3 Passive temperature stabilization

Moving further inside the cavity system, we encounter the Zerodur spacer that again sits on four Viton pads. Just as before, extrusions serve to reference the Zerodur spacer to the inside of the copper box. The low thermal expansion coefficient of Zerodur provides a stable environment for the cavity. On the top side, the Zerodur spacer has a raised ledge with square extrusions to mark the supporting positions which were calculated to make the cavity insensitive to vibrations.

The raised ledge also serves as a reference for the radiation shield. The radiation shield is made from a sheet metal copper alloy EN CW008A. The shield should act as a passive part to reduce thermal energy transfer to the cavity via radiation and to homogenize temperature. To work well as a radiation shield, the shield must have a very low emissivity  $\epsilon$ , which is a measure of how well the surface emits or absorbs thermal radiation. While a black body radiator would have  $\epsilon_{\text{Bb}} = 1$ , a polished copper surface may achieve an emissivity as low as  $\epsilon_{\text{Cu}} = 0.012$ . The radiation shield is made out of two parts and is designed to cover most of the solid angle around the cavity.

### 4.2.4 ULE-cavity

Here, I report on the same cavity spacer as in Nejc Janša's master thesis (Ref. [26]), but with different mirrors. After assembling the whole system for the first time, we measured a decrease of the cavity finesse. The manufacturer replaced the old fused silica mirrors with ULE-mirrors and remeasured the zero-crossing temperature. Details are given below in Section 4.3.3. The following paragraph describes the latest version of the cavity.

The ULE-cavity was bought from Stable Laser Systems (SLS) and manufactured by Advanced Thin Films (ATF). SLS provided us with a measurement of the zero-crossing temperature which was measured to be 33 °C. For our model (ATF-4020-4), the supporting positions that make the spacer insensitive to vibrations were calculated to be separated by 28.5 mm. The spacer has a diameter of 50 mm and the mirrors are separated by 100 mm, giving a free spectral range of  $\nu_{\text{FSR}} = 1.5$  GHz. One of the mirrors is plane while the other has a radius of curvature of  $R = 500$  mm. The mirrors are made on a ULE substrate and are coated to have a finesse of approximately 280 000 at 689 nm and 698 nm. The ULE-cavity sits on a set of four Viton pads, making it in total three stages of rubbery material that can effectively dampen vibrations.

## 4.3 Assembling the cavity

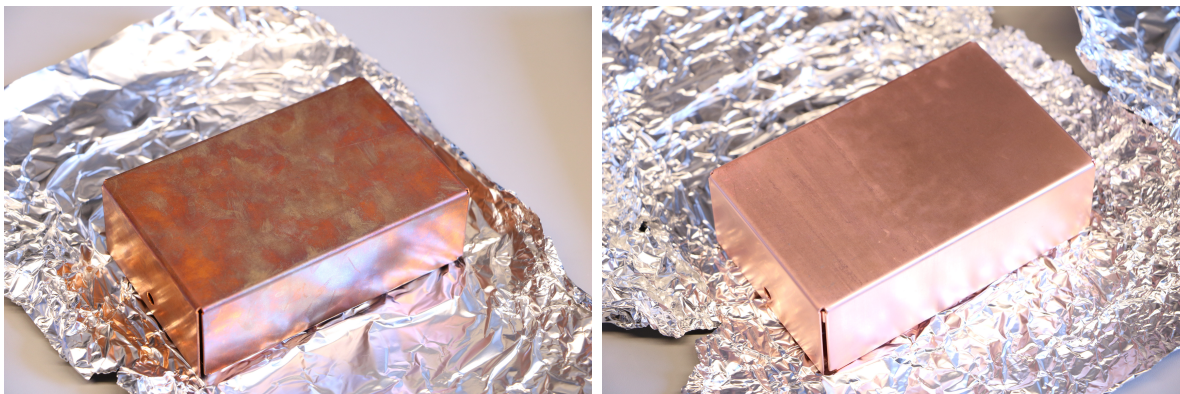
Because the cavity housing is evacuated, great care must be taken during the assembly of the different parts. Any contamination could ruin the vacuum. Therefore one should always wear appropriate gloves when dealing with vacuum components and maybe even a hairnet. Furthermore it is recommended to prepare and clean all the tools that one is going to use before breaking vacuum. This measure limits the risk of contaminating the vacuum accidentally and reduces the overall time that the chamber is exposed to air.

### 4.3.1 Cleaning vacuum parts

Prior to assembling the cavity, all parts were separately cleaned using a standardized procedure. A lot of useful information and tips on cleaning vacuum parts can be found in Ref. [33].

After the components arrived from the machine shop, every side was wiped with isopropanol to get rid of machining particles, grease, and oil. When any visible dirt was removed from the parts, they were placed into an ultrasonic bath. The ultrasonic bath is filled with deionized water and Liquinox, a vacuum cleaning soap made by Alconox. After the parts were sonicated for 10 minutes at 40 °C, they were taken out of the bath and were flushed with deionized water to wash off the soap. We flushed every side of each part for approximately 10s to make sure that all the soap was gone. After flushing, we took special care to not touch the parts without gloves, and we avoided touching the surfaces which are exposed to vacuum. Then, every side of each component was rinsed with acetone, quickly followed by a rinse with isopropanol to wash off everything before the acetone evaporates. Afterward, the parts were again flushed with deionized water and were placed on a sheet of fresh vacuum aluminum foil for drying. If the part contains threads or other small openings, we blew the part off with dry nitrogen. The alternative was to omit the last flush with deionized water so as not to have the risk of water being stuck. As soon as the parts were dry, we wrapped them in aluminum foil and loaded them into the oven. The baking should evaporate leftover solvents and water that still resides at the surfaces of the parts. The aluminum foil should help to keep the parts clean after taking them out of the oven to reduce the overall exposure to air. Good timing is essential, because leaving the parts outside vacuum for weeks would undo most of the positive effects of baking. We placed the parts into the vacuum not later than one day after baking.

Copper surfaces oxidize rapidly and after the radiation shield arrived from the machine shop oxidized fingerprints were visible spread all over the surface. A first baking in our oven made the situation even worse, because afterward the surface of the shield was strongly oxidized. The problem is that if the surface of the copper is not polished, its emissivity is not  $\epsilon_{\text{Cu}} = 0.012$ , but closer to  $\epsilon_{\text{Cu,oxidized}} = 0.78$ . To remove the oxide layer, we used citric acid. First, the surfaces were wiped off and then the shield was left over-night in a citric acid solution. To improve the radiation properties further, the shield was sent to plasotec GmbH, a company for plasma polishing. The difference can be seen in Figure 4.3. Baking the shield without oxidizing the surfaces again was problematic. We did not want to omit baking, so we decided to bake the shield under an Argon atmosphere. Therefore, I packed the radiation shield in aluminum foil, filled the package with argon before closing it, placed the two parts into our oven, and afterward flushed the whole oven with argon. The oven has two valves and a volume of 0.16 m<sup>3</sup>. I filled the oven from the lower valve while the upper valve was open. I set 0.5 bar on the pressure regulator which is connected to the lower valve by a 10 m long tube with 4 mm diameter. Using Poiseuille's equation for compressible fluids, we can derive a total Argon flow of about 10 times the oven volume, within 20 minutes. Then I closed the upper valve and lowered the pressure difference to a little bit above one atmosphere, while baking over night at 130 °C. The result looked



(a) Radiation shield after the first bake.

(b) Radiation shield after plasma cleaning.

Figure 4.3: Radiation shield before and after plasma cleaning.

promising, although you could see small oxidized fractions which I attribute to oxygen that was stuck in the aluminum foil package.

For synthetic material we did not use acetone because it dissolves most synthetic materials. Kapton is not problematic and one should use acetone to wash off the labels of the heating tapes. None of the electronic parts went into the sonicator.

### 4.3.2 Assembling the parts

When I joined the lab, the vacuum chamber was already partly assembled. The aluminum chamber, the copper box, and the stainless steel components with the ion pump were already in place. Back then, a pressure gauge was installed on one end of the 5-way cross. The radiation shield and the cavity were not yet implemented, nor were the heating elements or thermistors glued onto the copper box.

Before trying to glue heaters and thermistors directly on the copper box, we decided to prepare a test piece to check the vacuum compatibility of all the components. Therefore, we took a piece of copper of the same alloy as the copper box and glued a Kapton heating tape and a thermistor on the test piece. We used EPO-TEK<sup>®</sup> H77, a thermally conductive glue with low outgassing properties. This glue is electrically insulating, so gluing the thermistors into their designated holes does not create any shorts between their uninsulated leads. Special care was taken to not create any air bubbles below the heating tapes or in the thermistor holes to prevent virtual leaks. Especially the heating tapes can suffer from a bad thermal contact in the presence of bubbles. Locally they could get hotter than intended and start outgassing. It was hard to keep the heating tape in place, because the glue only sticks after we cured it at 130 °C in the oven. For the final round, it was necessary to use special weights that keep them in place. For the thermistors, we brought aluminum foil into the right shape to support them. After placing the test piece into the chamber and connecting the electrical parts to the D-sub feed through, we could evacuate the chamber. The pressure reached  $2 \times 10^{-6}$  mbar, which was the same value as without

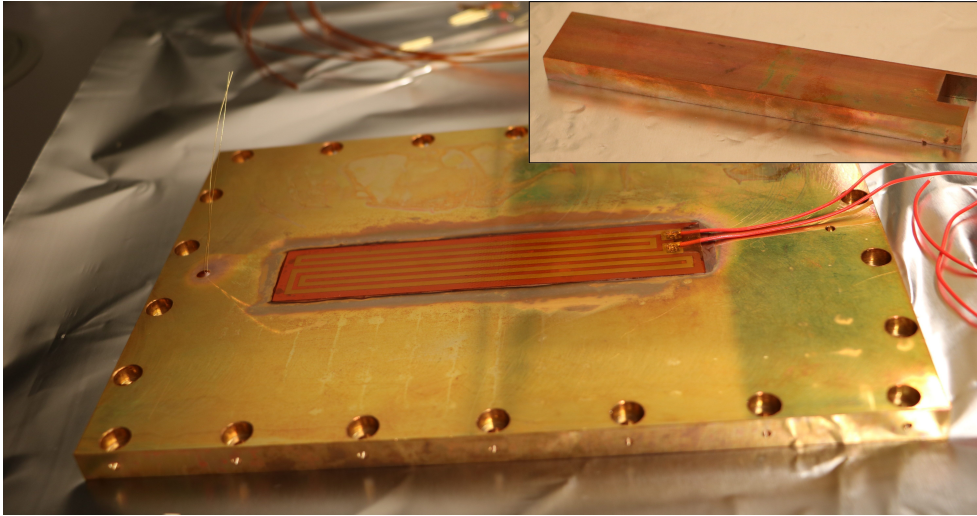


Figure 4.4: One side of the copper box before the copper box was assembled. On the left end you can see the leads of the thermistor and in the middle a Kapton heating tape was glued onto the copper surface. The inset shows the weight that was used to keep the heating tape in place during the curing step in the oven.

the test piece. Even ramping up the temperature of the test piece to  $49.6\text{ }^{\circ}\text{C}$  did not effect the pressure a lot. We concluded that all pieces were vacuum compatible and proceeded with the assembly.

We started with the copper box. After disassembling we could glue the thermistors and the heating tapes. This time we used a copper block with the same geometry as the heating tapes to ensure they stay in place and lie flat on the surface. The result looked promising (see Figure 4.4).

Wiring the thermistors and heating tapes was a bit problematic. Unfortunately it is not possible to just solder the connections, because the flux contained in the soldering tin would contaminate the vacuum. We used screw connectors, made out of an beryllium-copper alloy. They were quite heavy and not insulated, so we had to ensure that even after years of operation, gravity would not pull them down and create a short by touching a metallic surface. Ceramic beads of different sizes were used to insulate the bare thermistor leads and to secure the screw connectors. The heating tapes were delivered with Teflon insulated wires. Although Teflon should be fine for high vacuum, we decided to keep the insulation as short as possible to limit the overall amount of synthetic material inside the chamber.

The Fabry-Perot cavity was not unpacked until shortly before putting the cavity into place. As the positioning points were not referenced to the cavity, we used a ruler to find the correct position and checked carefully that the spacer does not touch the radiation shield at any point (see Figure 4.5). The venting hole of the cavity was initially closed with a piece of Kapton tape. The tape was removed only just before placing the cavity into the vacuum chamber. After putting the Zerodur spacer with cavity and the bottom

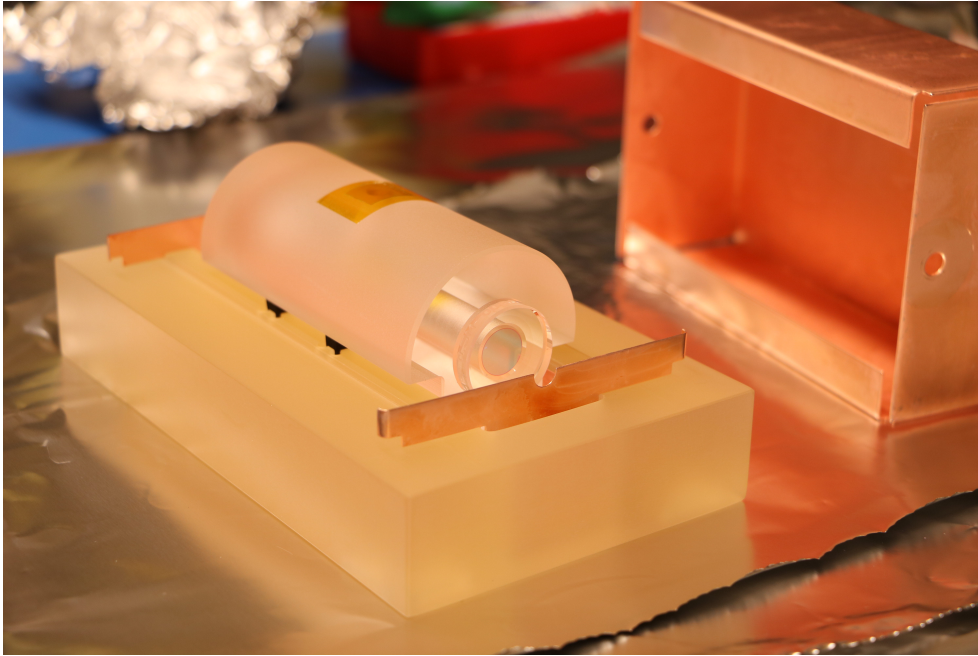


Figure 4.5: The Fabry-Perot cavity sits on the Zerodur spacer, supported by Viton pads in a way that make the cavity insensitive against vibrations. In the front you can see the bottom part of the radiation shield.

part of the radiation shield into the desired place, the top part of the radiation shield was carefully put in place. When the copper box was closed, only the wires had to be connected to the electrical feedthrough while using ceramic beads (see Figure 4.7). As a final step the whole chamber could be closed up.

The membrane and turbo pumps evacuated the chamber and within a day the pressure inside the chamber went down to  $2 \times 10^{-6}$  mbar. To further reduce the pressure, we baked the whole chamber. Baking evaporates the water that still resides on the surfaces inside the chamber. The pumps can then remove the water and the vacuum quality increases. Thermocouples were attached to the chamber and the chamber was wrapped with aluminum foil. A layer of heating wires provide the necessary thermal energy. The heating wires are followed by a layer of aluminum foil, fiber glass and another layer of aluminum foil to thermally isolate the chamber from the outside world. The chamber was then baked for two weeks at  $130^\circ\text{C}$ . The initially implemented pressure gauge broke during baking and could not be used any more. Fortunately, the ion pump can display the pressure calculated from its current, which dropped to  $4.8 \times 10^{-8}$  mbar after two more days.

### 4.3.3 Mirror contamination and second attempt

When the optical setup was ready to do initial measurements, we observed that the finesse of the cavity was lower than what it was supposed to be. Stable Laser Systems specified

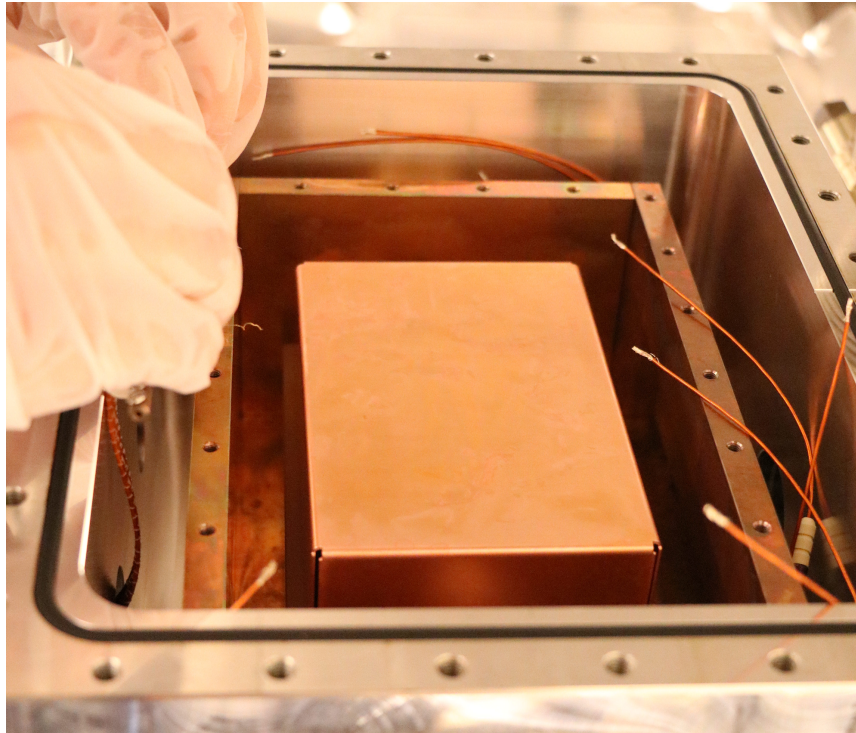


Figure 4.6: The radiation shield is in place.

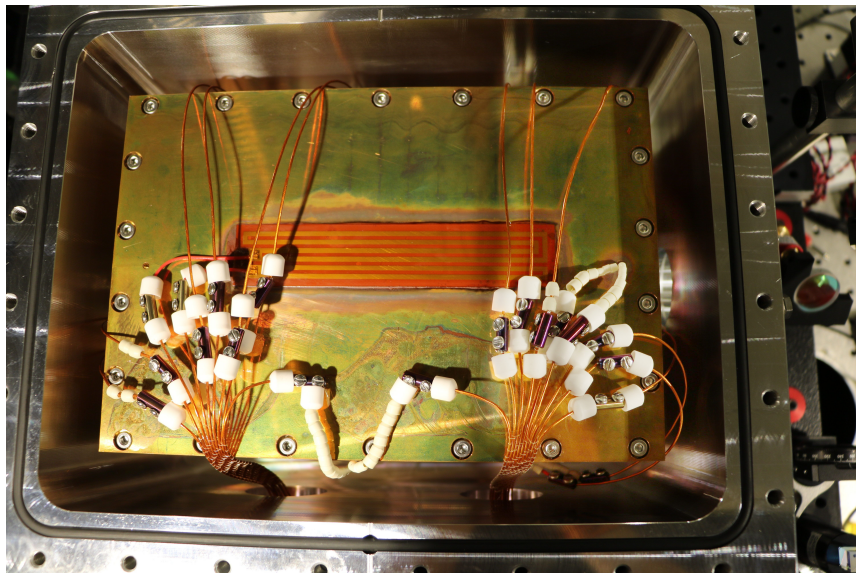


Figure 4.7: The final assembled copper box. White ceramic beads in different sizes are used to insulate the bare thermistor leads and the screw connectors from each other and the metallic surfaces. The screws were tightened as tightly as possible to ensure they would not get loose over time.

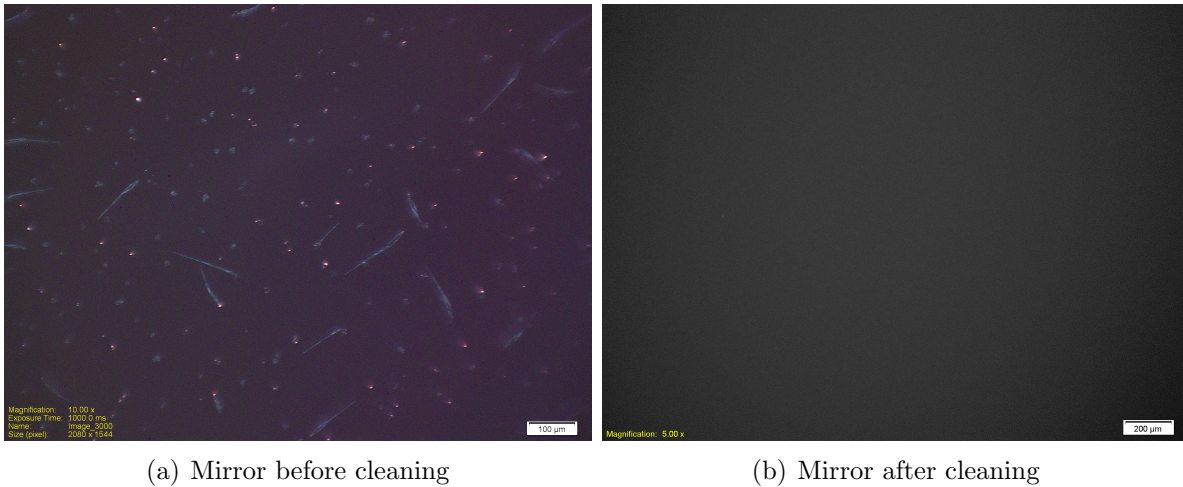


Figure 4.8: Image of the contaminated mirrors before and after they were cleaned.

a cavity finesse of more than 200 000, but we measured 65 000 (see Figure 2.7 for the ring down measurement). We concluded that at one of the performed steps, the mirrors were contaminated which led to the decrease in finesse. Therefore, we disassembled the cavity again and sent the Fabry-Perot resonator back to the manufacturer who cleaned the mirrors for us. Figure 4.8 shows pictures of the mirrors before and after they were cleaned. The mirrors looked very dirty initially. Cleaning removed the visible dirt, but the finesse did not improve. Stable laser systems provided us with a new pair of mirrors, which already were described in section 4.2.4.

As we did not know what exactly caused the decrease in finesse, we decided to repeat the procedure with a few changes. While the resonator was in the US for repairs, we baked the vacuum housing again for two weeks at 130 °C with the turbo pump attached. We hoped to get rid of any contaminant that still remained inside the cavity housing. When the optical resonator with the new mirrors arrived again, we flushed the chamber with argon, removed the broken pressure gauge to limit the total amount of elements attached to the cavity, and placed the optical resonator back in its place. Before pumping down the chamber, we measured finesse of the cavity to be 280 000 for 689 nm with a swept ring down measurement and obtained the specified finesse. We remeasured the finesse after each pumping step to exactly track what is happening. With the ion pump, we went down to  $8 \times 10^{-8}$  mbar and the finesse remained high. This time the last baking step was omitted, because we suspected that enhanced outgassing at high temperatures during baking could have caused the mirror contamination in the first place. When we turned on the heating tapes to stabilize the copper box to 33 °C the finesse dropped to  $\approx 270\,000$ . We concluded that the heating tapes were responsible for the loss in finesse and turned off the temperature control system.

## 4.4 Temperature stability

To stabilize the temperature of the copper box we used the digital controller PTC10 from SRS. In our configuration the PTC10 has two 50 W output channels and can monitor up to four thermistors simultaneously. The PTC10 features a proportional-integral-differential (PID) feedback loop, which can be tuned either manually or with the included feedback autotuner. I usually autotuned the system once in the beginning and a second time after the copper box settled to the desired temperature.

The measurements presented in this section were done with the first version of the cavity. For the old cavity SLS measured a zero-crossing temperature of 49.6°C. Therefore the measurements performed here were done at 49.6°C and not at 33°C, which is the zero-crossing temperature of the new cavity version.

### 4.4.1 Characteristic cooling time

Similar to a low-pass filter in an electric circuit, our cavity housing works as a low-pass filter for temperature fluctuations. N. Janša used this analogy in Ref. [26] to calculate theoretically up to which Fourier frequency temperature fluctuations are rejected by the low-pass characteristics of the vacuum housing itself. The characteristic time constant  $\tau$  is the time it takes until an object of initial temperature  $T_{\text{initial}}$  has reached  $1/e$  of the initial value. The theoretical result was a time constant of 69 h between the copper box and the aluminum chamber. After the cavity was assembled we could measure the time constant. We heated the copper box to 49.6°C and left the box at this temperature for a week to let the system equilibrate. Then we suddenly turned off the heaters. We used the data to fit a function of the form

$$T(t) = (T_{\text{initial}} - T_{\text{Room}})e^{-t/\tau} + T_{\text{Room}} \quad (4.7)$$

with  $T_{\text{initial}} = 49.6^\circ\text{C}$  and where  $T_{\text{Room}} = 21.6^\circ\text{C}$  is the final temperature. The fitting result can be seen in Figure 4.9, from which we obtain  $\tau = 20.6(7)$  h. Although the measured  $\tau$  is smaller than calculated, the result is very promising. We can assume that the characteristic time constant for the optical resonator is far bigger than 20.6 h, probably exceeding 24 h. This means that the daily temperature fluctuations are highly suppressed and do not significantly influence the temperature of the cavity.

### 4.4.2 Temperature stability

To find the best temperature stability we tried different heater configurations. In all configurations the thermistor glued to the bottom was used to control the heaters. We wanted the bottom part of the copper box to have the best temperature stability, because of its vicinity to the optical resonator.

The first configuration had all four heating elements connected in series. Thus the bottom temperature of the copper box was very stable, with a root mean square (rms) deviation of  $\Delta T_{\text{rms,bot}} \approx 0.4$  mK from the set point during one day, while the outside of the

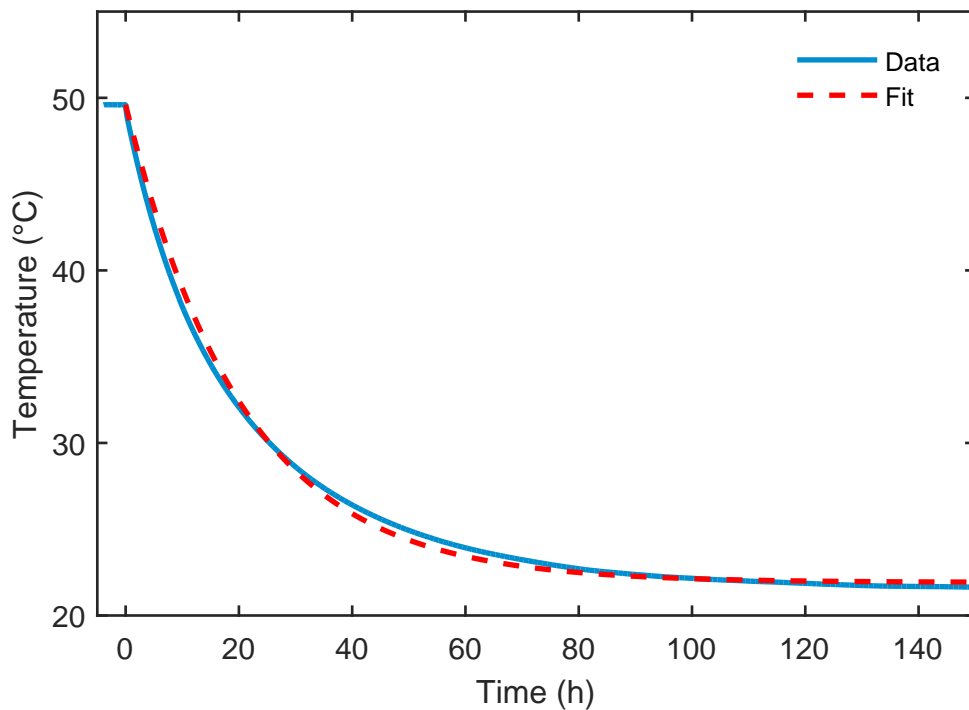


Figure 4.9: A dissipation of heat measurement of the copper box. The copper box was heated to  $49.6^{\circ}\text{C}$  and then heaters were shut down. The solid blue curve is the measured data. The dashed red line is Eqn. (4.7) fitted to the data, using  $\tau$  as fitting parameter. The fit revealed  $\tau=20.6(7)$  h.

aluminum chamber had an rms deviation of  $\Delta T_{\text{rms,out}} \approx 64 \text{ mK}$  from the mean value. At the top of the copper box (the most distant thermistor to the controlled bottom thermistor) we measured a variation of  $\Delta T_{\text{rms,top}} \approx 12 \text{ mK}$ .

The second heater configuration was to only use the bottom heating element. The deviations from the mean value during one day [ $\Delta T_{\text{rms,bot}} \approx 0.4 \text{ mK}$ ,  $\Delta T_{\text{rms,top}} \approx 8 \text{ mK}$ ,  $\Delta T_{\text{rms,out}} \approx 70 \text{ mK}$  (Fr., 07.04.2017)] were similar to the deviations in the former configuration. We settled on the second heater configuration.

In Figure 4.10, we heated the outside of the aluminum vacuum chamber with a heat gun by  $13^\circ\text{C}$  to see how a disturbance affects the temperature of the copper box, while all heaters were connected in series. The bottom thermistor reacts with a two-minute time delay and the disturbance is highly dampened. Interestingly, at the same time the temperature measured by the thermistor on the top of the copper box dropped by more than  $100 \text{ mK}$ . The reason is, that as soon as the bottom thermistor senses the disturbance, the PTC10 shuts down all the heaters. A similar effect can be seen every day in the morning when the first person enters the lab and turns on the light. The bottom thermistor senses a small temperature variation and tries to compensate for it, leading the top of the copper box to heat up when the lab cools down and vice versa. This behavior justifies the construction of an acoustic shield around the whole chamber, which would reduce the effect of room light on the cavity and further decouples the chamber from temperature variations in the lab.

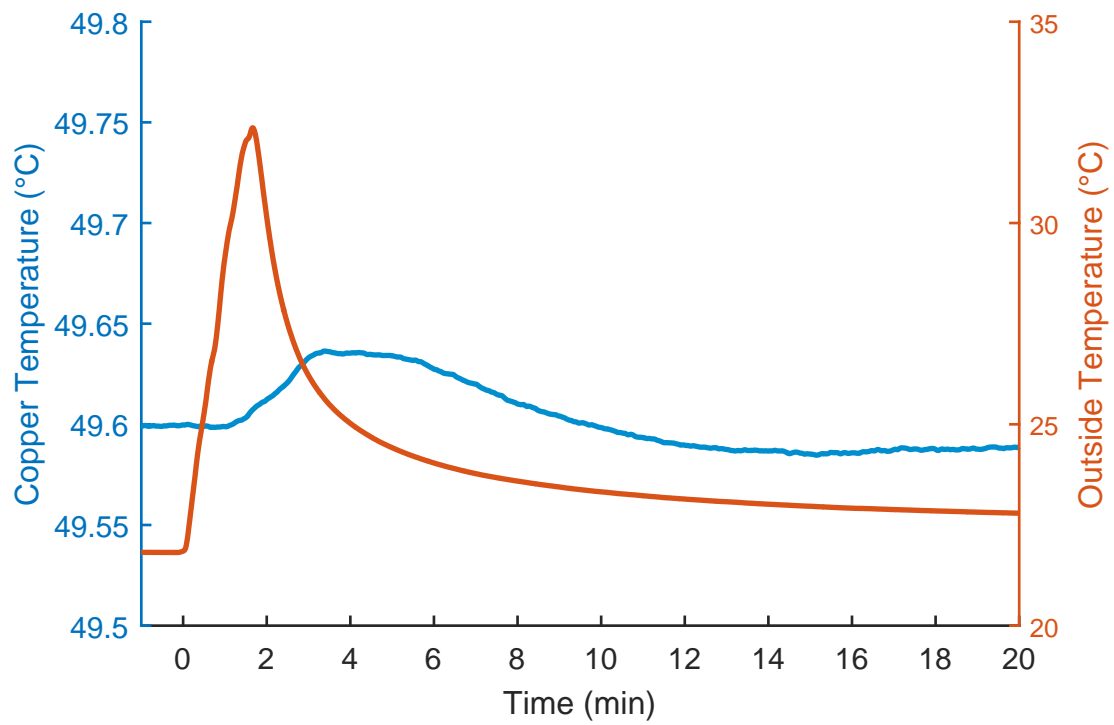


Figure 4.10: Temperature response of the copper box to an external perturbation. The aluminum chamber is heated, and only two minutes later the thermistor on the bottom of the copper box responds.

# Chapter 5

## Locking procedure and results

### 5.1 Optical setup and components

The components for the optical setup have to be chosen carefully and should be optimized for stability and low distortion of the beam quality. At the same time they must be small, because the space on the breadboard is limited. To make full use of the given space, we decided on a beam height of 4 cm. At 4 cm, we could still use the standard pedestals to mount optics, but at the same time the beam could pass below the mechanical components of the cavity. The whole setup can be seen in Figure 5.1. With this setup it is possible to lock both lasers (689 nm and 698 nm) to the cavity. Their beam path is almost identical, so we use the 689 nm beam path (displayed in red) as an example to go along the beam path step-by-step and look at all components we use:

The beam emitted by the laser is coupled into a fiber. This fiber is special because it contains an electro-optic modulator (EOM). The fiber-coupled EOM (“fiber EOM”) was bought from JENOPTIK (model number PM705). To work with a fiber-EOM is very convenient for several reasons. First, the polarization inside the polarization maintaining fiber is already very well aligned to correct crystal axis. Second, the EOM does not have a resonant circuit inside. Therefore we do not have to care about impedance matching the applied RF-signal. Another great feature is the small transverse size and the long interaction area, i.e. the long crystal length, which leads to a low half wave voltage. The half wave Voltage  $V_\pi$  is defined as the voltage that needs to be applied to the EOM to shift the phase of the light by  $\pi$ . The fiber EOM PM705 achieves a  $V_\pi$  as low as 4.2 V. The fiber attached to the EOM has a mode field diameter (MFD) of 4.4  $\mu\text{m}$ .

The light leaves the fiber using a customized out-coupler, which is optimized for stability. The lens used (Melles Griot, part number 06GLC001) has a focal length of  $f_1 = 6.5$  mm and is glued into a rotatable mount. By rotating the mount the fiber-lens distance can be adjusted to collimate the laser beam. Collimation was done with a shearing interferometer [34] located approximately 160 mm away from the out-coupler. Although the mounted lens fits tightly inside the rotatable mount, the small degree of freedom is enough to cause the beam leaving at an angle, which needs to be compensated.

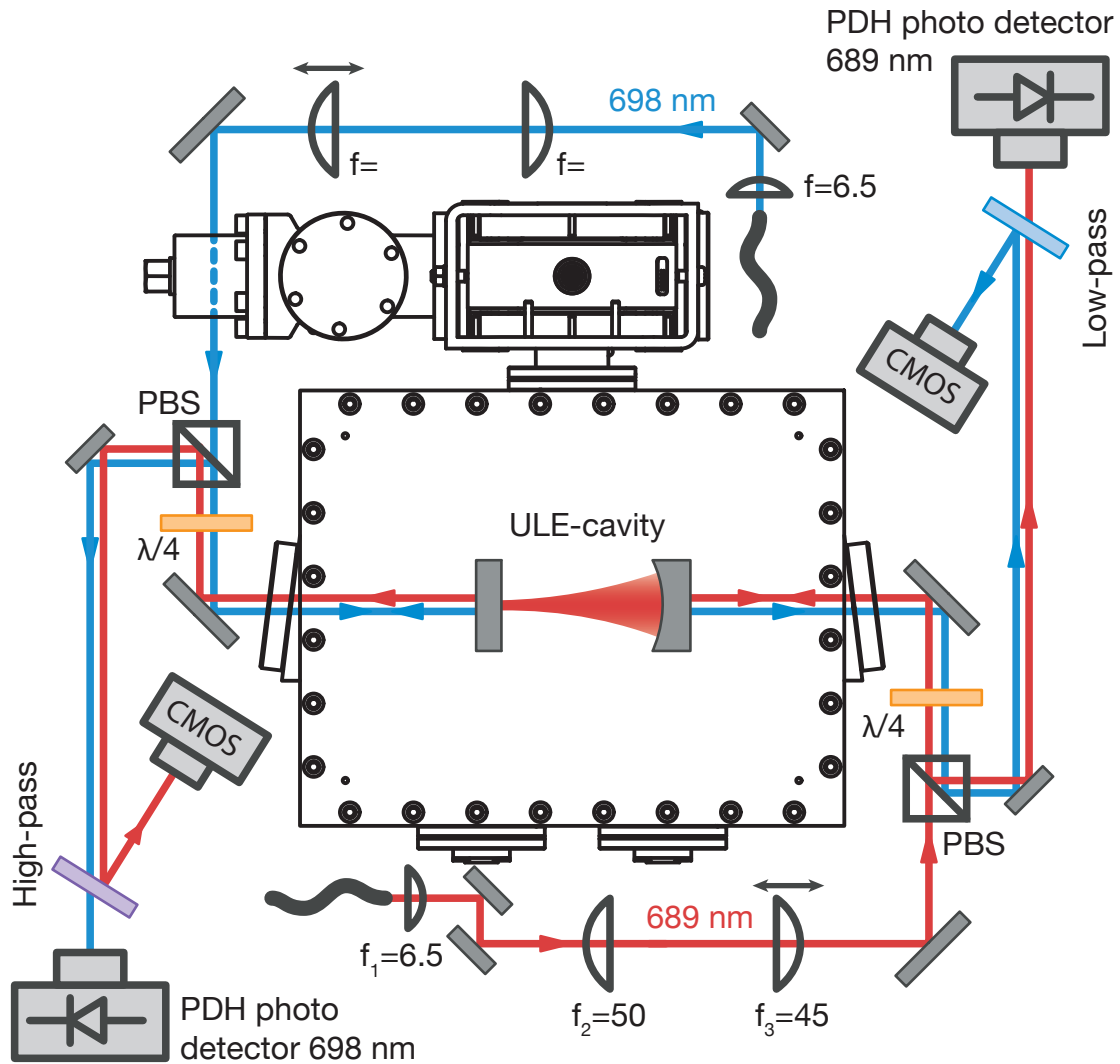


Figure 5.1: Optical setup on the cavity. The 698 nm beam is displayed in blue and the 689 nm beam in red to make them easy to distinguish. The fiber EOMs are also located on the vibration isolation stage but are not displayed.

To correct the beam path we placed two mirrors after the out-coupler. We used half inch mirrors (Thorlabs BB05-E02) to save space. The mirrors were mounted in Polaris mirror mounts (Thorlabs POLARIS-K05S2) because of their good stability properties. I adjusted these two mirrors such that the beam propagates along the desired optical axis, which is very important for the following telescope.

The telescope consists of two achromatic lenses with focal lengths  $f_2 = 50$  mm and  $f_3 = 45$  mm. They are used to “shape” the incoming beam such that the outgoing beam has perfect overlap with the beam that is resonant with the optical resonator. To avoid beam distortion, the beam should pass perpendicularly to the surface and through the center of the lenses. For this purpose, the orientation of the lenses to each other is fixed by mounting them on a cage system. Two irises on the front and on the back of the cage system made sure that the beam passes through the center of the lenses. The second lens is mounted in a translation stage to allow for fine adjustment of the beam shape. How the ideal focal lengths of the two lenses and their distance to each other were determined in a later a later section on mode-matching.

Three mirrors in total are used to couple the beam into the cavity. This time we used 1” mirrors with two monolithic Polaris mirror mounts (Thorlabs POLARIS-K1S5 and Thorlabs POLARIS-K1S4) because of their even better long-term alignment stability. The third mirror is fixed in a custom periscope that is designed to adjust the beam height to the height of the optical resonator (see Figure 5.2 for a render/photo of the mirror mount). The two mirrors in the POLARIS mounts are used for mode-matching the beam to the cavity. One of the mounts is screwed directly to the custom mount, which features alignment pins to ensure a  $45^\circ$  orientation of the mirror mount. This mirror mount was also chosen to have three adjustment knobs. The third knob gives us the necessary degree of freedom to also adjust the mirror plane to match the optical axis of the cavity.

Both the  $\lambda/4$  waveplate and the polarizing beam splitter are necessary to detect the reflected signal from the cavity. The waveplate, which also is mounted on the custom mount, transforms the incoming s-polarized light into circularly polarized light. When the beam is reflected at the cavity, the light passes again through the waveplate and transforms it into p-polarized light which is afterward reflected from the polarizing beam splitter (PBS). A final mirror guides the reflected light towards an optical “short-pass” filter that separates the transmitted light from the 698 nm beam from the 689 nm beam. This filter (Semrock, Versa Chrome TSP01-704) is a special optical element that transmits shorter wavelengths. The cutoff wavelength is very steep and can be tuned by changing the angle of incidence on the filter. For example at an angle of incidence of  $24^\circ$  the transmission of 698 nm is suppressed by more than 6 orders of magnitude, while more than 99% of the 689 nm passes through. A good filter is important, because we do not want any other light signal on the fast PDH photo detector that could disturb the error signal. After the filter a lens (not displayed) focuses the beam onto the fast PDH photo detector.

On the other side of the cavity, the transmitted light also transforms into p-polarized light and is picked of by a PBS. This time, the 689 nm beam is reflected on a long-pass filter (Semrock, Versa Chrome TLP01-704) and guided on a CMOS camera. During alignment it is a good idea to use a non-polarizing 50:50 beam splitter in front of the camera. The



Figure 5.2: A render of the custom mirror mount with optics.

beamsplitter allows to simultaneously observe the transmission on a camera and a high gain photo detector. The camera is necessary to identify the different TEM modes and to make sure that we are locking the laser to the fundamental TEM<sub>00</sub> mode.

## 5.2 Mode-matching

In Chapter 2 we have learned that a paraxial laser beam can exist in different TEM modes. We will call the modes which are resonant with the Fabry-Pérot resonator the eigenmodes of the resonator. Figure 5.3 shows the transmission signal of the Fabry-Pérot resonator while the laser frequency is swept over a FSR. The eigenmode transmission peaks are clearly visible and the camera tells us which peak corresponds to which mode.

The incident laser beam comes from a polarization-maintaining single-mode fiber and leaves the fiber in the TEM<sub>00</sub> mode. The term “mode-matching” describes the process of shaping the incoming beam such that the beam has maximal overlap with the TEM<sub>00</sub> eigenmode of the cavity. We use the telescope to transform the  $q$ -parameter of the incoming laser beam into the correct shape and use the two “coupling” mirrors in front of the cavity to align the incoming beam to the optical axis of the Fabry-Pérot resonator.

In section 2.5 we have evaluated the eigenmodes of a plano-concave resonator and found that the beam waist forms at the plane mirror and can be calculated from Eqn. (2.35). With this information, Eqn. (2.20) and the ABCD-law [Eqn. (2.32)] we are able to calculate the  $q$ -parameter of the cavity eigenmode at any point on the optical axis. For the incident beam we can look up the MFD of the optical fiber. In analogy to the beam radius of a Gaussian beam, half of MFD is the radial distance to the optical axis of the fiber after

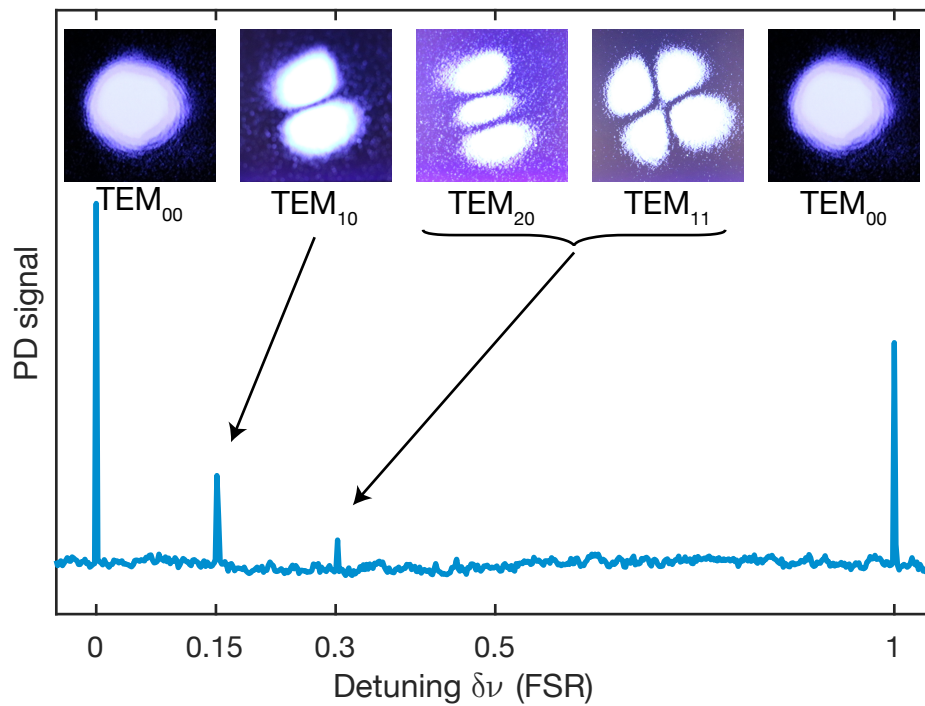


Figure 5.3: Transmission signal on a photo detector while scanning the laser frequency over one free spectral range. With the camera we can identify the single modes. The two outer peaks correspond to the  $TEM_{00}$  mode. We can also identify the  $TEM_{10}$ ,  $TEM_{20}$  and the  $TEM_{11}$  mode, while the last two modes are degenerate in frequency. The frequency spacing between the  $TEM$  modes is  $0.15 \times FSR$ .

which the electric or magnetic field has decayed to  $1/e$  of its peak. Therefore the MFD is equal to twice the beam waist of the incoming laser beam at the position where the beam leaves the fiber. The MFD of the fiber is  $4.4\ \mu\text{m}$ , which allows us again to calculate the  $q$ -parameter of the incoming beam at every position on the optical axis.

To find the correct focal lengths of the lenses in the telescope we could proceed as follows: First, we decide on the position where we want to place the telescope. We can use the ABCD law and the transfer matrices in Table 2.1 to calculate the beam sizes of the incident beam  $w_1$  and the eigenmode  $w_2$  of the resonator. Then we take a pair of lenses whose focal lengths have the same ratio as the beam radii, so that  $f_1/f_2 = w_1/w_2$ . If we separate them by a distance of  $f_1 + f_2$ , the magnification of the two lenses is given by  $f_1/f_2$ , such that the beam size of the incoming beam matches the beam size of the eigenmode. Now we can experimentally vary the distance between the two lenses to optimize the coupling.

This method is easy to implement, but it might lack accuracy. More accurately we could write the beam waist of the incoming beam as a function of the distance between the lenses in the telescope. Knowing this function we can fit the incoming beam to the eigenmode by varying the distance in the telescope.

I calculated the best mode-matching for the setup seen in Figure 5.1. The experimental procedure to mode-match the incoming beam to the eigenmode of the resonator begins with looking at the reflected light from the cavity. For now I left the beam splitter disassembled and used the two coupling mirrors to overlap the incoming and the reflected beam. At the same time I adjusted the position of lens 3 such that the reflected beam had approximately the same size as the incoming beam. Then I started to scan the laser frequency with the internal piezoelectric transducer (PZT) and looked with the ccd camera for a transmission signal. For this adjustment it is helpful to turn off the light in the lab. If the reflected signal was adjusted carefully, seeing the first faint transmission signal is not so hard. In most cases this transmission is a high order TEM mode, which can be observed on the CCD camera. The next step is to beam-walk the two coupling mirrors to reduce the observed high order TEM mode to low order TEM modes until you find the TEM<sub>00</sub> mode. Now it should be possible to see the transmission signal by eye which helps a lot in guiding the transmitted light onto a photo detector. An example for the transmitted light signal can be seen in Figure 5.3.

The real work now is to iteratively improve the coupling efficiency to the TEM<sub>00</sub> mode. In other words, this means looking at the transmission signal and maximizing the TEM<sub>00</sub> mode while minimizing the peaks caused by all other modes. Before beginning we should recall the degrees of freedom we have to improve the coupling. First, we have the two mirrors for coupling. The mirror farther away from the cavity is used to adjust the optical axis and therefore is called “position mirror”. The mirror closer to the cavity (“angle mirror”) is then used to adjust the angle of the laser beam. The second degree of freedom is a third knob on the angle mirror. With this knob we can push the angle mirror back and forth to adjust to the optical axis. A last degree of freedom arises from the second lens in our telescope. We mounted the second lens on a translation stage in the cage system. Moving the lens alters the beam size and the position of the beam waist. My strategy for

mode-matching included the following three steps:

1. Improve mode-matching by altering the position and the angle mirror simultaneously.
2. Move the position of the second lens in the cage system and repeat step 1. If the situation improved, proceed by moving the lens further in the same direction. If the coupling became worse, try the other direction. In the first iterations I did quite large steps of about half a centimeter and marked the positions on the rods of the cage system. Later I used the fine adjustment screw for precise alignment. From the coupling efficiency we can infer information on the beam size: If we couple to high-order modes which have larger radial size, the beam waist is probably too large. The lens should then be moved closer to the cavity.
3. In the end also the third knob of the angle mirror can be used to match the beam to the correct optical axis. Together with the other two knobs, the mirror can be pushed back and forward. After each change in the third knob, step one must be repeated.

## 5.3 Electronics and setting them up

For successful locking of the laser to the cavity we also require electronics. We used a home-built fast photo detector and two units from Toptica, the PDD/F for deriving the error signal and the FALC 110 as loop filter.

### 5.3.1 Photo detector

The home built photo detector was built according to the schematics and description of the electrical circuit in Ref. [26]. The photo diode inside the detector transforms the incident light power linearly into a current  $I_{\text{PD}}$ . This current is then transformed into a voltage  $V_{\text{PD}}$  that can be read off by e.g. a scope. The gain  $R_G$  of the photo detector is a resistor inside the circuit that determines the transfer ratio:

$$V_{\text{PD}} = R_G I_{\text{PD}}. \quad (5.1)$$

The larger  $R_G$  is, the more sensitive the photo detector becomes. Unfortunately, with high gain the bandwidth of the photo detector shrinks. The bandwidth of a photo detector determines up to which frequencies the PD is capable to resolve modulations. As we have seen in section 3.2 the photo detector must at least be able to resolve frequencies up to the modulation frequency  $\Omega$ . So the proper gain is a trade off between making the photo detector as sensitive as possible and still having a bandwidth far above  $\Omega$ . For stabilizing the 689 nm laser I used the photo detector marked SW01 with a gain of  $R_G = 2.49 \text{ k}\Omega$  which results in a bandwidth of more than 50 MHz.

### 5.3.2 PDD 110/F

The reflection signal of the photo detector is then fed into the Pound-Drever-Hall detector PDD 110/F. The PDD 110/F features all the required electronics to create an error signal. Figure 5.4 shows a picture of the front panel of the PDD 110/F and the internal schematics. The schematics consist of two branches. The upper branch starts with the internal oscillator signal which is adjustable between 12 MHz and 35 MHz. We set the modulation frequency to  $\Omega = 20.3$  MHz, because this frequency was the resonance frequency of the EOM we used before the fiber EOM arrived and then we stayed with 20.3 MHz for now. The oscillator signal passes through an amplifier that can be manipulated on the front panel to adjust the signal at the oscillator output between 0 and  $1 V_{pp}$ . This output is then connected to the EOM that modulates the phase of the light incident on the cavity. I tried to set the amplification such that the sidebands in the through the cavity transmitted light signal contain  $\sim 40\%$  of the carrier power. At this ideal value the discriminator has the steepest slope (see Ref. [23]).

The lower branch begins with the photo detector input. Here the cavity reflection signal of the the fast photo detector is fed in (“PD input”). A high pass filter removes the DC-part of the reflection signal. Before the signal is mixed with the oscillator signal the PD signal can be amplified (“gain”-knob). According to the manual the photo diode input signal should be between  $10 mV_{pp}$  (maximal gain) and  $1 V_{pp}$  (minimal gain). Afterward the mixer produces the error signal. Notice that the following  $510 k\Omega$  resistor and capacitor C32 (1 pF) form a low pass filter with a bandwidth of 312 MHz. This low pass filter cannot filter out the sum frequency  $2\Omega$ . The intention is to not limit the response to the bandwidth of the low pass filter. The sum frequency is then sufficiently suppressed by the low pass characteristics of the control servo and the laser diode itself. A phase shifter (“Phase”-knob) allows to correct for phase delays that occur in the circuit. I adjusted the phase by only looking at the error signal on the scope through a 2.5 MHz low pass filter to suppress the sum frequency. By turning the “Phase”-knob I tried to maximize the central peak of the error signal. Figure 5.5 shows the resulting error signal measured with a scope.

### 5.3.3 FALC

We used the FALC 110 from Toptica as a loop filter. Its task is to take the error signal from the PDD 110/F and calculate a response which is then fed into the laser head to counteract frequency changes. Figure 5.6 shows the front control panel of the FALC. The error signal is fed into either the inverting (“invert”) or the non inverting (“noninv”) input to achieve negative feedback. Otherwise the FALC tries to lock the laser to one of the sidebands. One should consider to feeding the error signal via a coupler into the FALC input. A coupler is an electrical device which has an input, an output and a “coupled” port. Most of the input signal is fed through to the output, but a fraction is sent to the coupled port. With the coupled port we are able to observe the error signal on a scope and simultaneously maintain the  $50 \Omega$  environment.

After the signal passes through the input section, the circuit of the FALC splits into

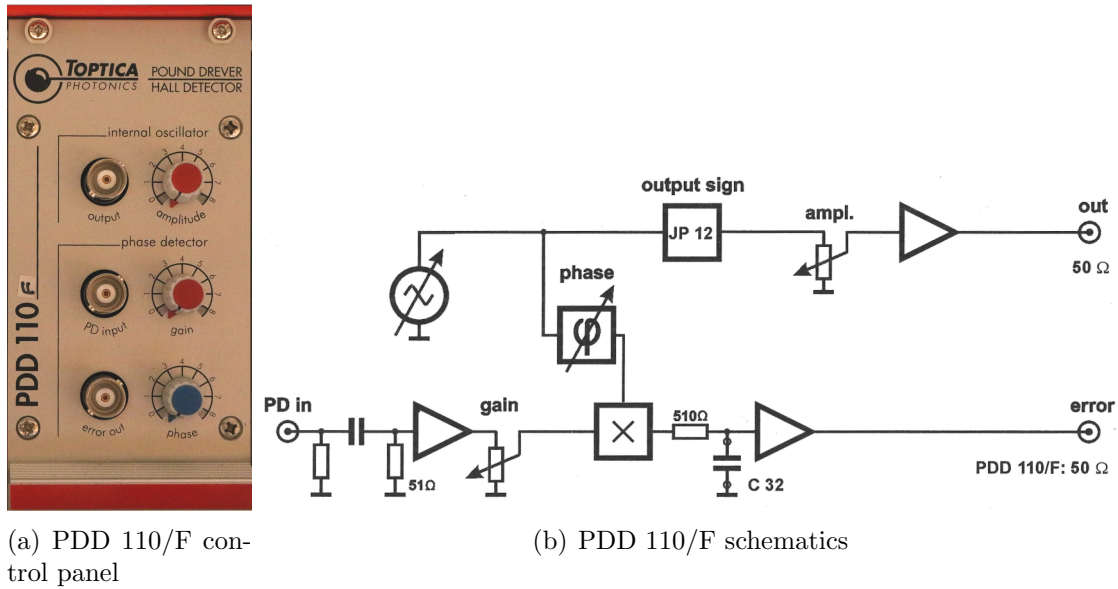


Figure 5.4: Pictures of the control panels of the (a) Pound-Drever-Hall detector PDD110/F and (b) its schematics (taken from Ref. [35]).

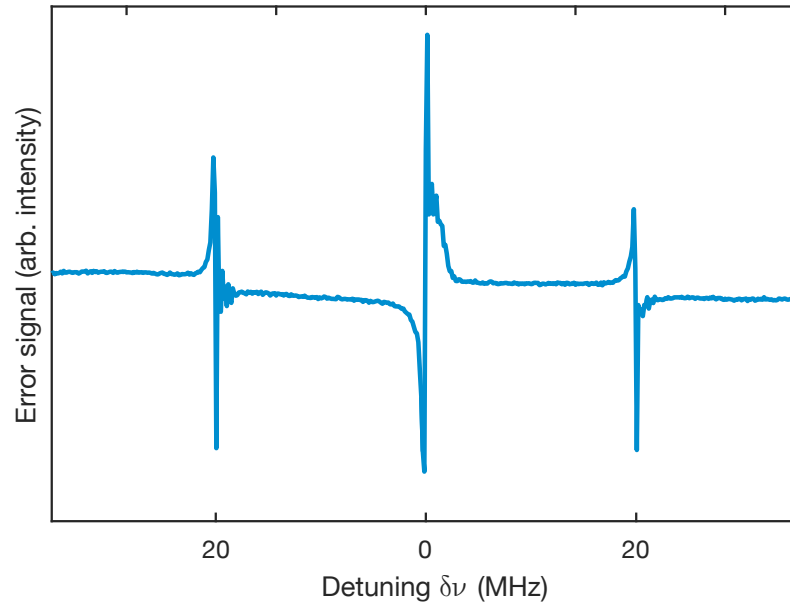


Figure 5.5: An error signal produced with the PDD 110/F. The modulation frequency is  $\Omega = 20.3$  MHz.

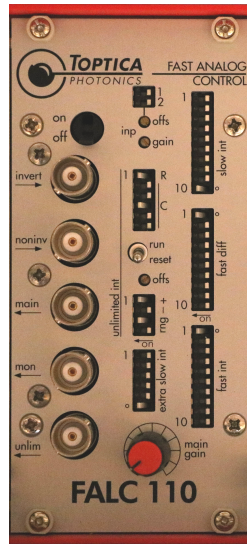


Figure 5.6: A picture of the FALC front control panel.

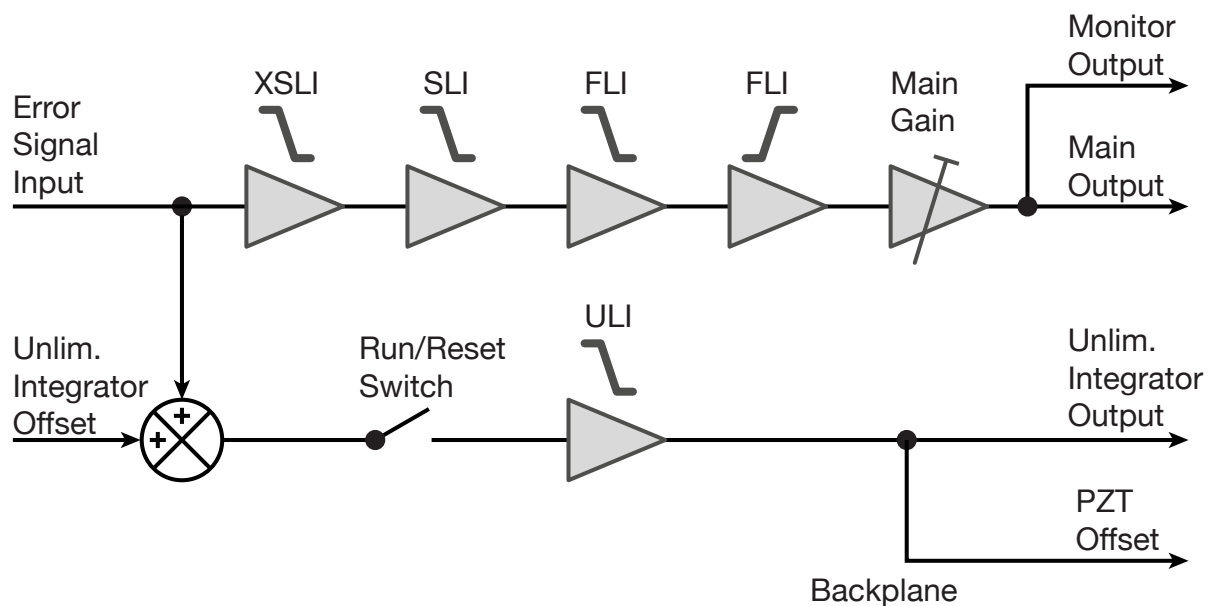


Figure 5.7: Simplified FALC 110 block diagram. For a more detailed block diagram see Ref. [36]. The error signal is split into two parts, the fast circuit branch (top) and the unlimited integrator (bottom).

two branches (see also the block diagram in Figure 5.7):

- The fast circuit branch takes over high frequency disturbances by modulating the laser diode current.
- The unlimited integrator (ULI) branch with a high DC gain should take over low frequency drifts with larger amplitude. Via the backplane, the FALC is connected to the PZT actuator. Modulating the PZT is slower than modulating the laser current, but the PZT covers a higher frequency range.

Separating these two branches has the advantage that we can set up the lock with the fast branch only and the ULI turned off. This makes locking easier, because the high DC gain of the ULI would send the frequency of the laser very far off if the laser frequency does not sit on the error signal slope.

We will first have a look at the fast circuit branch. The fast circuit branch consists of three integrators (called extra slow, slow and fast limited integrators, XSLI, SLI and FLI, respectively) and one differentiator (called fast limited differentiator, FLD). Their individual transfer functions can be changed with the corresponding DIP switches on the front panel. Essentially with the DIP switches one chooses between different capacitor values for the integrators and the differentiator. As a result, both of their gain slopes are along the frequency axis. They can also individually be turned off (unity gain) using the DIP-switch marked with a 0.

To achieve the first lock I followed the instructions in Ref. [36, p. 26]. This instruction describes for instance how to adjust the input offset to the correct value. The general procedure is then to set the correct parameters for the integrators and the differentiator and connect the main output (“main”) to the DC modulation input of the laser head with the main gain potentiometer turned completely counterclockwise. Then we scan the laser frequency with the PZT over a resonance of the cavity, while watching the error signal and the “Monitor Output” of the FALC on a scope. By slowly raising the main gain potentiometer we suddenly see how the FALC tries to hold on to the error signal slope. Decreasing the scan amplitude further towards zero and simultaneously adjusting the frequency of the laser should result in a locked laser via the fast circuit branch. One can adjust the laser frequency using either the PZT offset or the laser diode current, but for fine adjustment the current should be used because it is more sensitive. The remaining question left is how could we find good starting parameters? In my judgment, good starting parameters were FLI=9 and SLI=6, whereas the XSLI and the FLD were turned to a flat response (XSLI=6, FLD=1). This resulted in a gain of 52 dB for frequencies  $f < 200$  Hz and 15 dB for  $f < 3$  kHz, respectively. With those parameters I achieved a lock that lasted several minutes. It is a good idea to attach the error signal from the coupler to a spectrum analyzer, which is very helpful in analyzing which frequencies are suppressed very well and which are not. One can try to set the FLI to higher frequencies, letting the SLI follow.

As soon as we have achieved locking the laser with the fast circuit branch we can start to set up the unlimited integrator branch. To this end, we connect the unlimited output

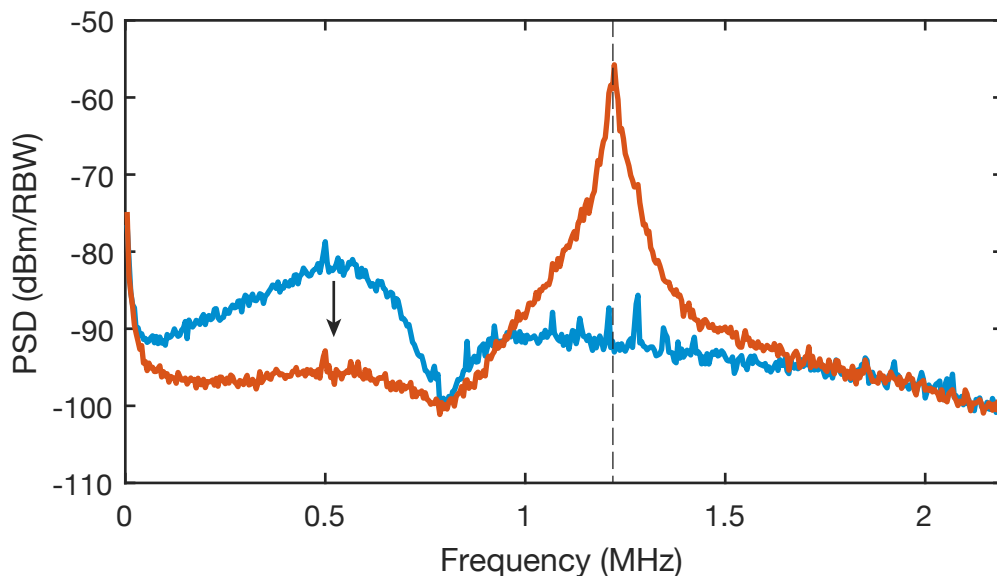


Figure 5.8: The plot shows the power spectral density of the error signal, while locking the 689 nm laser to the old  $\mathcal{F} = 65\,000$  cavity. The controller bandwidth at 1.2 MHz is indicated with a dashed line.

“unlim” to a scope. Good starting parameters are found in Ref. [36, p. 27]. The main task is to set the offset of the unlimited integrator branch to the correct value. We first lock the laser with the fast circuit branch and then activate the unlimited integrator. Probably the laser will then fall out of lock because the unlimited integrator offset was not well adjusted. This unadjusted offset will cause the ULI to send a far too large signal to the laser and sends it off the error signal slope. Looking at the scope: if the unlimited integrator output rises (falls) we have to decrease (increase) the offset. We then repeat this procedure by continually adjusting the offset, until the laser does not fall out of lock after turning on the ULI. For fine adjustment I watched the transmission signal before I turned on the ULI. As soon as the ULI is turned on, its contribution pulls the transmission signal to a lower value. We adjust the offset slowly until we retrieve the old value for the transmission signal. This method ensures that we lock to the central frequency of the transmission peak.

When locking with the ULI is achieved, the ULI takes over the low frequency parts. Now we can try again to maximize the bandwidth of the lock using the fast branch. To do so I tried to iteratively push the FLD to the maximum followed by the FLI and then by the SLI, while watching the error signal on the spectrum analyzer. The spectrum analyzer was set to a resolution bandwidth (RBW) of 100 Hz. The reference level was 0 dBm and the detection method was rms. The result can be seen in Figure 5.8, where the effect of the lock becomes evident. The blue curve shows the power spectral density with a low overall gain. By raising the overall gain (orange curve) we see that frequencies in the kHz range are suppressed as indicated by the arrow. At the same time, the bandwidth of the controller at 1.2 MHz becomes visible.

This whole procedure resulted in stable lock. Locking times of several hours were achieved and the lock is insensitive against vibrations. The lock was stable enough to withstand vibrations that arise from hitting the surface of the optical table with a screwdriver. Such stability is desirable, because it allows working at the laser table without unlocking the laser.



# Chapter 6

## Unibody Littrow Laser

In addition to my main project of locking a laser to an ultrastable reference cavity, I also worked on a project of building an external cavity diode laser. The goal of the project was to have a simple laser design with which we can build lasers with a large variety of different wavelengths. Ideally we would have a ready construction set and just have to assemble the parts. The “Unibody Laser” design [37] from the Steck Lab seems to fit our requirements. This laser was originally constructed for cooling strontium and thus the components for the wavelengths we are interested in are readily available.

This chapter starts with a brief introduction on diode lasers, followed by a report on constructing a laser. The main focus lies on the selection criteria of the different parts.

The laser I constructed has a nominal wavelength of 632.8 nm. This wavelength is special for strontium, because an optical lattice composed of light with  $\lambda=632.8$  nm can capture atoms in the  $5s^2\ ^1S_0$  state, but results in a plane potential landscape for atoms in the  $5s5p\ ^3P_0$  state [38]. This wavelength is therefore called a “magic-zero” wavelength.

### 6.1 ECDL

Semiconductor lasers are one of the most common sources of coherent laser light. In semiconductor lasers, the radiation is created by interband transitions of electrons from the conduction band to the valence band. This transition happens in a confined area, which is enclosed between two partially reflective surfaces (“mirrors”). Those surfaces (or laser facets) form an optical resonator. For us it is enough to treat a laser diode (LD) as an optical resonator, which encloses a gain medium. As a light field bounces back and forth between the cavity mirrors, it passes through the gain medium several times and gets coherently enhanced.

The LD chip in which this amplification process happens is usually quite small, and the cavity lengths are in the 100–1000  $\mu\text{m}$  range. This small resonator size results in a cavity with a rather low  $Q$ -factor. Hence, the resonances of the cavity are very broad and result in a laser linewidth of typically several 10–200 MHz [39].

One simple approach to narrow down the linewidth is to extend the cavity length. One

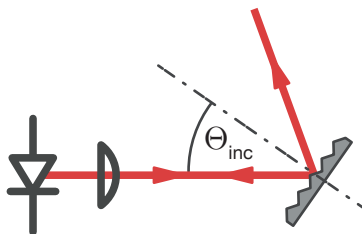


Figure 6.1: Schematic representation of the Littrow configuration. A grating works as frequency selective element and the first diffraction order is reflected back into the LD. The undiffracted beam leaves the resonator and is used as laser beam.

can think of building an external cavity around the LD, which is formed by one of the LD facets and an external mirror. The result is called an external cavity diode laser (ECDL), where the LD chip is used as gain medium. Using a frequency dependent external mirror brings the additional benefit to be able to tune the laser frequency.

The most common choice as external mirror is an optical grating. A grating is an optical element, which diffracts light according to the grating equation

$$\sin \Theta_{\text{inc}} - \sin \Theta_m = mg\lambda, \quad (6.1)$$

where  $\Theta_{\text{inc}}$  is the angle of incidence and  $\Theta_m$  is the angle of the diffracted light ray. Both are measured with respect to the grating normal, but have a different sign. The other parameters are the wavelength  $\lambda$  and the grating constant  $g = 1/d$ , which is the reciprocal of the spacing between the single grooves. The light is diffracted into several orders, labeled with the integer diffraction order number  $m$ .

In the Littrow configuration, which is depicted in Figure 6.1, the first diffraction order is reflected back into the laser diode. This means that  $\Theta_{m=1} = -\Theta_{\text{inc}}$  and we arrive at the Littrow equation

$$\sin \Theta_{\text{inc}} = \frac{g\lambda}{2}. \quad (6.2)$$

## 6.2 Components

The individual components and the laser design are already very well described in Ref. [37]. What follows is a brief description of the most important design features as well as a more intense focus on the components we have chosen individually for every laser with different wavelength. These are the laser diode and the grating. In Table 6.1 we list wavelengths for which we plan to build a Littrow laser and give suggestions for components to achieve them. In this section we also discuss the selection criteria and how we decided on these LD and grating combinations.

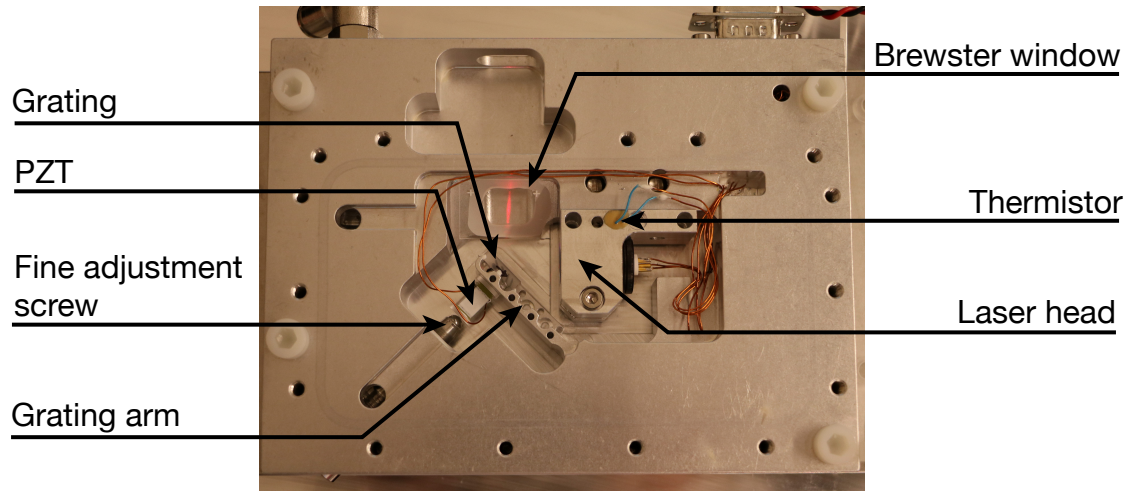


Figure 6.2: A picture of the Littrow laser.

Figure 6.2 shows a picture of my completed laser with a peak wavelength at 632.8 nm. The LD is fastened in the laser head and emits light towards the grating. A highlight is the diffraction grating arm, which holds the diffraction grating. The grating arm is designed to have low mass to avoid low-frequency mechanical resonances. Furthermore, it is formed out of the same piece of aluminum for good stability. The resonator is designed to have an angle of incidence (AOI) of  $45^\circ$  degrees onto the grating. With the fine adjustment screw we can push grating back and forth to adjust the AOI. Furthermore we can shim the grating to obtain an even larger AOI tuning range without bending the grating arm too much. In the end we will be limited by the geometry of the design. A beam of 2 mm diameter will be clipped before leaving the cavity if the AOI deviates more than  $3.5^\circ$  from the intended  $45^\circ$ .

The laser beam exits the chamber through a microscopy slide that we cut to the required size. The slide itself is mounted in Brewster's angle, so that light with an electric field vector perpendicular to the plane of the optical table (s-polarized light) is transmitted completely.

### 6.2.1 Choosing a laser diode

As we have seen in the discussion above, when building an ECDL we replace the small internal resonator of an LD by a larger one. Unfortunately, when we place an untreated LD in a larger resonator, we will end up with two resonators that compete against each other. If the feedback from the grating is not high enough, the internal resonator will dominate and we can not take advantage of the ECDL. On the other hand, if we increase the feedback by choosing a different grating, the resulting output power will suffer because more light is lost inside the resonator. The best performance and high output power can be achieved if we make the reflectivity of one of the facets of the LD bad before placing the

$\lambda$ (nm)	LD part nr. (supplier)	Grating part nr. (supplier)	$g$ mm <sup>-1</sup>	AOI
461	NDBA116T (Nichia)	263232-XX50-424 (Zeiss)	3000	43.8°
633	SAL-0635-010 (Sacher)	53-*-300R (Richardson)	2160	43.1°
679	0680007022000 (Eagleyard)	53-*-059H (Richardson)	2000	42.8°
688	0690007031000 (Eagleyard)	53-*-059H (Richardson)	2000	43.5°
689	0690007031000 (Eagleyard)	53-*-059H (Richardson)	2000	43.6°
698	SAL-0705-020 (Sacher)	53-*-059H (Richardson)	2000	44.3°
813	0840060101500 (Eagleyard)	53-*-136H (Richardson)	1714	44.2°
914	0920040101500 (Eagleyard)	53-*-239H (Richardson)	1500	43.3°
922	0920040101500 (Eagleyard)	53-*-239H (Richardson)	1500	43.8°

Table 6.1: Listed are the wavelengths for which we plan to build Littrow lasers and possible components. Next to possible LD and gratings with grating constant  $g$ , we also list the from Eqn. (6.2) resulting angles of incidence (AOI). The part numbers of LDs from Eagleyard are very long and are therefore listed only partially. To obtain the full number number, replace the symbol \*\*\* in EYP-RWE-\*\*\*-SOT02-0000 by the listed number.

LD into the larger resonator. Decreasing the reflectivity of a LD facet can be done with an anti-reflection (AR) coating. The authors in [39] explain how a LD can be AR coated. Anti-reflection coated laser diodes for ECDLs are commercially available, but expensive. The LDs listed in Table 6.1 feature an AR coating.

### 6.2.2 Grating

Selecting the right grating is very important and will have great influence on the laser performance. The most important selection criteria results from the laser geometry. In our laser the angle of incidence resulting from Eqn. (6.2) should be as close as possible to 45°, which is the intended position of the grating arm. This calculation already gives us an idea of what the grating constant should be. Then we can look in the manufacturer's catalogs to find a grating with a  $g$  close to the calculated value. Richardson Gratings provides a large number of standard gratings, and is therefore a good place to start any search. The next selection criteria is the diffraction efficiency into the first diffraction order of the grating. This efficiency is very sensitive to polarization, so most manufactures provide different data for the two polarization states. We are interested in s-polarization which transmitted through the Brewster window without losses. Here we need to be careful, because the definition of the polarization can easily lead to great confusion. We usually define s- and p-polarized light as light with electric field vectors that are perpendicular and parallel to the plane of incidence, respectively. Grating manufactures often define S- and P-polarized light as light with perpendicular and parallel electric field vectors, with respect to the grating groves. I used small and capital letters to distinguish between them, but when looking for gratings one should always check which convention is used. It is not always easy to tell what the correct amount of feedback should be. The gratings used in Ref. [37] provide feedback in the range between 16% and 25%. Too high feedback limits

the output power of the laser, but too low feedback leads to a dominant internal resonator. Sometimes, an upper limit is set by the LD itself. In case of the NDBA116T from Nichia, the datasheet [40] provides an upper limit of 30% feedback, because higher feedback would damage the front facet of the LD. For an AR coated LD, a feedback in the range between 15% and 30% should be a good choice. For a laser diode without AR coating, we should consider to increase feedback.

## 6.3 Construction

The construction of the Littrow laser is already well documented with assembly pictures on the Steck Lab webpage [41]. Here I want to give general assembly tips and report on slight changes that we performed. Moreover, shortly after I built my laser I supervised the construction of a second laser for 698 nm. Lukas Homeier joined our group as a Bachelor student to write his Bachelor thesis [42] on the construction of a Littrow laser. In his thesis he also describes every construction step.

Throughout the entire construction phase, participants should wear gloves to avoid any contamination. This precaution can potentially eliminate a problem that happened in another lab that built a Littrow laser using the same design. Within two months, the laser became contaminated with a thin layer on the grating. The grating was no longer able to provide the desired feedback and therefore had to be exchanged. Although the exact cause of the contamination in the other lab was never determined, we should be especially careful to keep the interior of the laser clean.

### 6.3.1 Assembling tips

Prior to assembling, all the parts underwent the same cleaning procedure as described in section 4.3.1, except that we did not bake the parts. For gluing all the different parts, we used Torr Seal instead of Epo-Tek 353ND. Torr Seal is also suitable for most vacuum applications, but in contrast to Epo-Tek 353ND, Torr Seal cures at room temperature and has a high viscosity. We took care to not close up the laser before the glue completely dried. With this method we hoped to avoid any contamination by an evaporating component of the glue. Also we tried to limit the total amount of glue. Usually already small amounts of glue are enough to keep the parts in place. The thermistor was the only element that was glued with EPO-TEK H77, because we wanted to ensure a good thermal contact between the thermistor and the laser head.

When stripping the Kapton wires one should be careful where the Kapton flakes land. They like to stick to the wire, so I recommend to clean off every wire before closing the laser. Especially the wires lying above the Brewster window should be carefully cleaned, because Kapton flakes landing on the window could distort the beam.

When placing the grating, it is very helpful to have a second assisting person who holds the laser block such that one can slide the grating onto the grating arm. Otherwise it can easily happen that the grating falls over on the grating side and gets damaged.

We realized that screwing the top part to the laser body influenced the performance of the laser. We attribute this effect to wires inside the cavity that are moveable. Their movement is transferred to the laser diode and may change the alignment. A solution could be to glue the wires at fixed positions to the laser body, which stabilizes the wire positions. The top part of the laser body features an extrusion at the position where the laser head sits to avoid touching the cables. In future designs we should enlarge this extrusion such that it stretches over the whole interior.

# Chapter 7

## Conclusion

### 7.1 Summary

I built an ultrastable frequency reference housing which provides a  $< 1$  mK temperature stable environment. The characteristic cooling time of the actively temperature stabilized part was measured to be 20.6 h, which indicates a high decoupling from external temperature fluctuations. Moreover, the housing provides good vibration isolation. All of the components used inside are vacuum compatible, so we could achieve a pressure stability of  $10^{-8}$  mbar measured over a period of 24 h.

It became apparent that one or more of the components used inside the housing caused a contamination of the resonator mirrors. The contamination resulted in a loss in finesse of the resonator to a level which was too low to achieve a laser linewidth in the Hz range. With new mirrors we found that the loss in finesse happens as soon as the heating tapes are turned on. We concluded that three components were potentially responsible for the loss in finesse: the glue, the Kapton heating tapes or the Teflon insulated wires that came with the heating tapes. Each of these components should be replaced in future cavity housing designs.

The current finesse was measured with several ring-down measurements and determined to be  $\sim 270\,000$ . We left the heating elements turned off so as not to ruin the finesse again. Observing the finesse for a period of two weeks did not reveal a change in finesse. We conclude that the contamination of the mirror only happens when the heaters are turned on.

The 689 nm laser could be locked to the ultrastable cavity, using an commercial loop filter. The resulting lock is stable against vibrations and lasts for several hours. With the commercial loop filter we achieved a bandwidth of 1.2 MHz.

With the Littrow laser design, we provide a complete set of instructions and components that allows the construction of similar lasers for a variety of wavelengths. With the instructions, the laser is easy to set up and serves as a fast and cheap alternative to commercial diode lasers.

## 7.2 Outlook

At the moment it is not possible to actively temperature stabilize the frequency reference housing without risking to ruin the cavity mirrors again. Without the temperature stabilization to the zero crossing temperature it will not be possible to stabilize the laser against frequency drifts which are induced by thermal changes in the cavity. As a consequence, it is necessary to build a second ultrastable cavity. Alternatively, we could replace the temperature stabilized copper box. In either case, we should try to reduce the total amount of synthetic material inside the vacuum chamber and use a different glue. Here is a list of possible alternatives:

- Glue: Torr Seal does not have as good thermal properties but should work without contaminating the mirrors.
- Heating elements: thermoelectric elements do not contain polymers. They have the additional advantage to work either as heating or cooling elements depending on the sign of the applied current.
- Viton seals: we had to use Viton gaskets and O-rings because aluminum is too soft to use copper gaskets. An alternative would be to use indium seals. Indium is softer than aluminum and a bare wire between two aluminum surfaces would serve as a very good seal. In contrast to Viton gaskets, noble gases can not penetrate through a metal, which results in a better vacuum.
- Kapton insulated wires: instead of insulated wires we could use bare wires which we insulate with ceramic beads.

The inclusion of a second ultra stable frequency reference would have several advantages. Firstly, we could compare the two references to each other. Therefore we lock two different lasers to each of the cavities and then look at their beat note signal, from which we can infer a reliable value for the laser linewidth. As a second advantage, we could measure the zero crossing temperature of each cavity. Stable Laser Systems provided us with a measurement of the zero crossing temperature of our cavity spacer, but the measurement was done with another pair of mirrors. The zero crossing temperature also depends on the CTE of the Mirrors, because mirrors with a different CTE than the spacer material can shift the zero crossing temperature. Although our mirrors are made of ULE glass we should remeasure the zero crossing temperature, because the CTE of ULE spacer or substrates depends also on the batch of ULE glass from which they were made [43].

A review of the project is only complete when it includes the successes and failures we experienced. I had to leave before the locking of the 698 nm laser was achieved. All the optics were set up, but there was not enough time to achieve the lock. The acoustic shield around the chamber was under construction, so it could not be installed and tested. The construction of the Littrow laser for 632.8 nm was completed and the laser worked, but its linewidth is not yet characterized. Furthermore, the mode-hop free tuning range has to be optimized.

This master thesis summarizes my projects and what I have learned. The goal of this thesis is to serve as a reference for future projects that include the ultra stable reference cavity or a Littrow laser that was built with the above described design.



# Bibliography

- [1] I. Bloch, J. Dalibard, and S. Nascimbene, “Quantum simulations with ultracold quantum gases,” *Nature Physics*, vol. 8, no. 4, pp. 267–276, 2012. DOI: 10.1038/nphys2259.
- [2] R. P. Feynman, “Simulating physics with computers,” *Int. J. Theor. Phys.*, vol. 21, pp. 467–488, 1982. DOI: 10.1007/BF02650179.
- [3] A. J. Daley, M. M. Boyd, J. Ye, and P. Zoller, “Quantum computing with alkaline-earth-metal atoms,” *Phys. Rev. Lett.*, vol. 101, p. 170504, 2008. DOI: 10.1103/PhysRevLett.101.170504.
- [4] A. V. Gorshkov, A. M. Rey, A. J. Daley, M. M. Boyd, J. Ye, P. Zoller, and M. D. Lukin, “Alkaline-earth-metal atoms as few-qubit quantum registers,” *Phys. Rev. Lett.*, vol. 102, p. 110503, 2009. DOI: 10.1103/PhysRevLett.102.110503.
- [5] A. V. Gorshkov, M. Hermele, V. Gurarie, C. Xu, P. S. Julienne, J. Ye, P. Zoller, E. Demler, M. D. Lukin, and A. M. Rey, “Two-orbital  $su(n)$  magnetism with ultracold alkaline-earth atoms,” *Nat Phys*, vol. 6, no. 4, pp. 289–295, 2010. DOI: 10.1038/nphys1535.
- [6] T. L. Nicholson, S. L. Campbell, R. B. Hutson, G. E. Marti, B. J. Bloom, R. L. McNally, W. Zhang, M. D. Barrett, M. S. Safronova, G. F. Strouse, W. L. Tew, and J. Ye, “Systematic evaluation of an atomic clock at 2 1018 total uncertainty,” *Nature Communications*, vol. 6, p. 6896, 2015. DOI: 10.1038/ncomms7896.
- [7] S. Stellmer, F. Schreck, and T. C. Killian, *Annual Review of Cold Atoms and Molecules*, vol. 2. World Scientific, 2014. ISBN: 978-981-4590-16-7.
- [8] H. J. Metcalf and P. van der Straten, “Laser cooling and trapping of atoms,” *J. Opt. Soc. Am. B*, vol. 20, no. 5, pp. 887–908, 2003. DOI: 10.1364/JOSAB.20.000887.
- [9] S. Stellmer, R. Grimm, and F. Schreck, “Production of quantum-degenerate strontium gases,” *Phys. Rev. A*, vol. 87, p. 013611, 2013. DOI: 10.1103/PhysRevA.87.013611.
- [10] W. Nagourney, *Quantum Electronics for Atomic Physics and Telecommunication*. Oxford Graduate Texts, OUP Oxford, 2014. ISBN 9780191643385.

- [11] H. Kogelnik and T. Li, “Laser beams and resonators,” *Appl. Opt.*, vol. 5, no. 10, pp. 1550–1567, 1966. DOI 10.1364/AO.5.001550.
- [12] M. Born and E. Wolf, *Principles of Optics: Electromagnetic Theory of Propagation, Interference and Diffraction of Light*. Cambridge University Press, 2000. ISBN: 9780521784498.
- [13] E. Hecht, *Optik*. Oldenbourg, 4 ed., 2005. ISBN: 9783486273595.
- [14] H. Roger A. Horn, *Topics in Matrix Analysis*. CAMBRIDGE UNIV PR, 1994. ISBN: 978-0-521-46713-1.
- [15] B. Saleh and M. Teich, *Fundamentals of Photonics*. Wiley Series in Pure and Applied Optics, Wiley, 2007. ISBN: 9780471358329.
- [16] D. J. McCarron, “A guide to acousto-optic modulators,” tech. rep., Durham University, 2007.
- [17] M. J. Lawrence, B. Willke, M. E. Husman, E. K. Gustafson, and R. L. Byer, “Dynamic response of a fabry–perot interferometer,” *J. Opt. Soc. Am. B*, vol. 16, no. 4, pp. 523–532, 1999. DOI: 10.1364/JOSAB.16.000523.
- [18] M. J. Martin, *Quantum Metrology and Many-Body Physics: Pushing the Frontier of the Optical Lattice Clock*. PhD thesis, University of Colorado, 2013.
- [19] R. W. Fox, C. W. Oates, and L. W. Hollberg, *Stabilizing diode lasers to high-finesse cavities*, vol. 40, ch. 1, pp. 1–46. *Experimental Methods in the Physical Sciences*, 2003. DOI: 10.1016/S1079-4042(03)80017-6.
- [20] J. L. Schiff, *Laplace Transform*. Springer New York, 2013. ISBN: 978-0-387-22757-3.
- [21] G. F. Franklin, J. D. Powell, and A. Emami-Naeini, *Feedback Control of Dynamic Systems*. Pearson Education Ltd, 7 ed., 2015. ISBN: 978-1292068909.
- [22] J. Bechhoefer, “Feedback for physicists: A tutorial essay on control,” *Rev. Mod. Phys.*, vol. 77, pp. 783–836, 2005. DOI: 10.1103/RevModPhys.77.783.
- [23] E. D. Black, “An introduction to Pound-Drever-Hall laser frequency stabilization,” *American Journal of Physics*, vol. 69, pp. 79–87, 2001. DOI: 10.1119/1.1286663.
- [24] D. Meschede, *Optics, Light and Lasers: The Practical Approach to Modern Aspects of Photonics and Laser Physics*. Wiley-VCH, 2007. ISBN: 978-3-527-40628-9.
- [25] S. B. Koller, J. Grotti, S. Vogt, A. Al-Masoudi, S. Dörscher, S. Häfner, U. Sterr, and C. Lisdat, “Transportable optical lattice clock with  $7 \times 10^{-17}$  uncertainty,” *Phys. Rev. Lett.*, vol. 118, p. 073601, 2017. DOI: 10.1103/PhysRevLett.118.073601.

- [26] N. Janša, “A frequency-stable diode laser system for spectroscopy and trapping of Sr atoms,” Master’s thesis, Ludwig-Maximilians-Universität München, August 2016.
- [27] Corning Advanced Optics, *ULE<sup>®</sup> Corning Code 7972 Ultra Low Expansion Glass*, 2008.
- [28] Schott AG, *ZERODUR<sup>®</sup> Zero Expansion Glass Ceramic*, 2014.
- [29] Schott lithotec, *Synthetic Fused Silica*, 2006.
- [30] Deutsches Kupferinstitut, *Werkstoff-Datenblatt Cu-OFE - CW009A*.
- [31] S. A. Webster, M. Oxborrow, and P. Gill, “Vibration insensitive optical cavity,” *Phys. Rev. A*, vol. 75, p. 011801, 2007. DOI: 10.1103/PhysRevA.75.011801.
- [32] F. Matichard, B. Lantz, K. Mason, and R. M. et al., “Advanced LIGO two-stage twelve-axis vibration isolation and positioning platform. part 1: Design and production overview,” *Precision Engineering*, vol. 40, pp. 273 – 286, 2015. DOI: 10.1016/j.precisioneng.2014.09.010.
- [33] K. M. Birnbaum, *Cavity QED with Multilevel Atoms*. PhD thesis, California Institute of Technology, 2005.
- [34] M. E. Riley and M. A. Gusinow, “Laser beam divergence utilizing a lateral shearing interferometer,” *Appl. Opt.*, vol. 16, no. 10, pp. 2753–2756, 1977. DOI: 10.1364/AO.16.002753.
- [35] TOPTICA Photonics AG, *Sys DC 110 Manual*, 09 ed., 2014.
- [36] TOPTICA Photonics AG, *FALC 110 Manual*, 03 ed., 2013.
- [37] E. C. Cook, P. J. Martin, T. L. Brown-Heft, J. C. Garman, and D. A. Steck, “High passive-stability diode-laser design for use in atomic-physics experiments,” *Review of Scientific Instruments*, vol. 83, no. 4, p. 043101, 2012. DOI: 10.1063/1.3698003.
- [38] M. S. Safronova, Z. Zuhrianda, U. I. Safronova, and C. W. Clark, “The magic road to precision.” arXiv, 2015. arXiv:1507.06570.
- [39] R. Fox, L. Hollberg, and A. Zibrov, “Semiconductor diode lasers,” in *Atomic, Molecular, and Optical Physics: Electromagnetic Radiation* (F. Dunning and R. G. Hulet, eds.), vol. 29, Part C of *Experimental Methods in the Physical Sciences*, pp. 77 – 102, Academic Press, 1997. ISBN: 978-0-12-475977-0.
- [40] Nichia, *Laser Diode NDBA116T*, 2016. Datasheet.
- [41] “Unibody laser assembly photos,” 2012. Online available: <http://atmoptics-nas.uoregon.edu/unilaser/photos.html>, Accessed on 05-Jun-2017.

- [42] L. Homeier, "Setup and characterization of a littrow laser for 689 nm." Bachelorthesis, 2017.
- [43] R. W. Fox, "Temperature analysis of low-expansion fabry-perot cavities," *Opt. Express*, vol. 17, no. 17, pp. 15023–15031, 2009. DOI: 10.1364/OE.17.015023.

# Acknowledgments

First of all, I would like to thank my supervisor, Sebastian Blatt, for all the guidance through the experiments that I have performed during my time at MPQ. Having an answer to every question, conversations with him about any topic are always full of insights. Furthermore, I would like to thank him for all the effort he spent in reading this thesis, spotting mistakes and teaching me a good style of writing.

I would like to thank Immanuel Bloch for the possibility to write my thesis in his group and for letting me partake in an awesome year full of science. I appreciate being able to participate in two conferences and the group retreat, as well as the possibility to work with high tech equipment in one of the leading research groups for quantum many-body physics.

The largest contributions to my good time here have are the other members of my team: André Heinz, Annie Jihyun Park, Stepan Snigirev, Fabian Finger, Lukas Homeier and Etienne. I enjoyed all our common dinners very much and I will miss the great atmosphere in the lab. I would especially like to thank our two PhD students: Andre Heinz for always being ready to have interesting conversations and a helping hand in my projects. Anni Park for always being very motivated and cheering me up when I was having problems and staying until late night to help me setting up the clock laser. Special thanks go also to Stepan Snigirev for always taking his time to fix my problems.

I would also like to thank the whole Bloch group for main contributions to my football table skills after lunge and after every cake session. Thank you all for the awesome evenings whenever we were at a conference. Especially I would like to thank Christoph Gohle, for everything he taught me about PDH-locking, and Marcell Duda, for never ending discussions about our Littrow laser projects.

I would like to thank further the technician of the group: Anton Meyer, Karten Förster and Olivia Mödl. Especially I want to thank Anton Meyer for being most helpful in technical questions, always taking his time to explain me things in detail and being essential in looking for pieces that nobody else would have know they even existed.

The great time I had in Munich I attribute to a very special person: Larissa Ermoschkin. Thank you so much for always cheering me up in rough times, for calming me down when I am restless and for providing me with new energy when I am exhausted. Talking to you opens new opportunities to me and converts every single moment into a great event.

I thank my entire family for all the support and never letting me feel alone, regardless of where I am.

# Erklärung

Hiermit erkläre ich, dass ich diese Arbeit selbstständig verfasst und keine anderen als die angegebenen Quellen und Hilfsmittel benutzt habe

---

Datum

---

Unterschrift